Journal of Hydrology 612 (2022) 128044

Contents lists available at ScienceDirect

Journal of Hydrology

journal homepage: www.elsevier.com/locate/jhydrol

Research papers

Global assessment of partitioning transpiration from evapotranspiration based on satellite solar-induced chlorophyll fluorescence data

Yaojie Liu [a,b,c], Yongguang Zhang [a,b,c,*], Nan Shan [d], Zhaoying Zhang [a,b,c], Zhongwang Wei [e]

[a] International Institute for Earth System Sciences, Nanjing University, Nanjing 210023, China
[b] Jiangsu Provincial Key Laboratory of Geographic Information Technology, Nanjing University, Nanjing 210023, China
[c] International Joint Carbon Neutrality Laboratory, Jiangsu, China
[d] Nanjing Institute of Environmental Sciences, Ministry of Ecology and Environment of the People's Republic of China, Nanjing 210042, China
[e] Southern Marine Science and Engineering Guangdong Laboratory (Zhuhai) & Guangdong Province Key Laboratory for Climate Change and Natural Disaster Studies, School of Atmospheric Sciences, Sun Yat-sen University, Guangzhou, Guangdong, China

ARTICLE INFO

This manuscript was handled by Emmanouil Anagnostou, Editor-in-Chief

Keywords:
Evapotranspiration partitioning
Transpiration estimation
Solar-induced chlorophyll fluorescence
Stomatal conductance
Penman-Monteith model

ABSTRACT

An accurate assessment of terrestrial ecosystem transpiration (T) is important to understand the vegetation-atmosphere feedbacks under climate change. Solar-induced chlorophyll fluorescence (SIF) shows great potential to estimate T because of its mechanical linkage with photosynthesis and stomatal conductance. However, a global and spatially estimation of terrestrial T based on remotely sensed SIF remains unresolved and novel strategies are challenged to entail a precise partition of T from evapotranspiration (ET) across various biomes. Here, with far-red SIF from Sentinel-5 Precursor satellite and ground observations for a total of 30 sites encompassing ten primary plant functional types (PFTs), we extend a SIF-driven semi-mechanism canopy conductance (g_c) model for different plant functional types (PFTs), and use the optimized Penman-Monteith model (PM_{opt}) to calculate T and T/ET. We reveal that the relationship between SIF and the product of g_c and 0.5 power of vapor pressure deficit ($g_c \times VPD^{0.5}$) is tighter than the relationship between SIF and ecosystem productivity. The SIF-$g_c \times VPD^{0.5}$ linear regressions show improved R^2 and increased magnitude in slopes across PFTs when aggregating daily to 16-day. Our T/ET results show high correlations with the results of the Ball-Berry-Leuning model combined with PM_{opt} at the site scale ($R^2 = 0.69$), and with the results calculated by leaf area index in a previous study at the PFT scale (0.70). We further determine the global mean T/ET (0.57 ± 0.14), close to the ensemble mean of global averaged T/ET (0.55), using 36 different methods. The global T estimated using the SIF-based approach is compared with two other remote sensing products. Our method provides a valuable tool for T and ET estimation using remote sensing data and is critical to understanding ecohydrological processes under climate change.

1. Introduction

Terrestrial Evapotranspiration (ET), a fundamental component of the terrestrial ecosystem water cycle, substantially influences climate change, water availability, and land surface energy balance (Milly et al., 2005; Trenberth et al., 2009; Zeng et al., 2017). The proportion of global precipitation returning to the atmosphere via ET is close to 60%, higher in arid and semi-arid zones (Mu et al., 2011). Different components of ET -interception evaporation (I), evaporation (E) and transpiration (T) - react to climatic changes, atmospheric composition, and land use differently (Wei et al., 2017). T is the primary component in ET that involves soil moisture uptake from the root and water vapor loss through plant stomates (Schlesinger and Jasechko, 2014). As T is directly linked to photosynthesis via stomatal conductance (g_s), it has long been acknowledged that quantification of T plays a crucial role in water resource management, crop yield estimation, water cycle, and climate change. However, it is still challenging to partition ET into its subcomponents at the regional and global scales. Significant variations in the ratio of T to ET (T/ET) have been reported from 47% ± 10% in the Mediterranean shrubland with low Leaf Area Index (LAI) to 70% ± 14% in the Tropical rainforest with high LAI (Schlesinger and Jasechko, 2014; Wang et al., 2014). Global estimates of T/ET vary from ∼ 35% to

* Corresponding author at: International Institute for Earth System Sciences, Nanjing University, Nanjing 210023, China.
E-mail addresses: liuyaojie@nju.edu.cn (Y. Liu), yongguang_zhang@nju.edu.cn (Y. Zhang), zhaoying_zhang@nju.edu.cn (Z. Zhang), weizhw6@mail.sysu.edu.cn (Z. Wei).

https://doi.org/10.1016/j.jhydrol.2022.128044
Received 30 September 2021; Received in revised form 29 May 2022; Accepted 4 June 2022
Available online 16 June 2022
0022-1694/

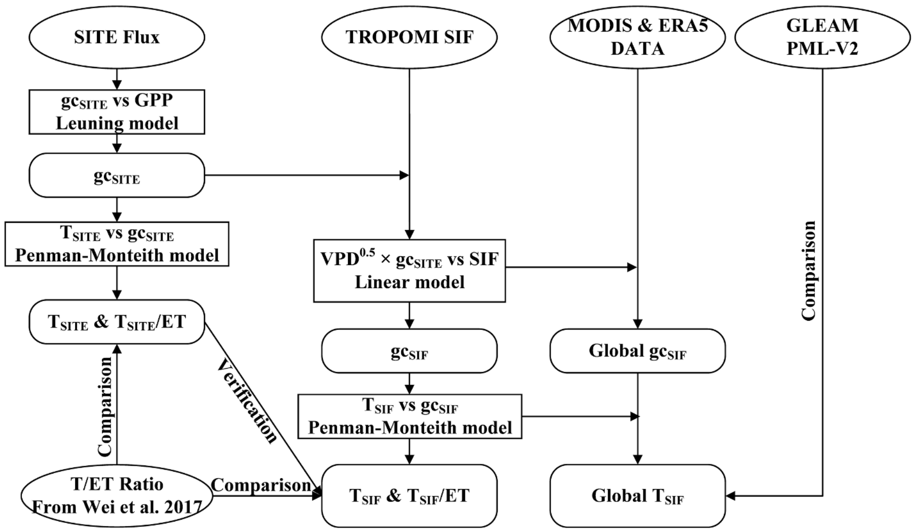

Fig. 1. The Workflow of this study.

~ 80% derived from different methods (Coenders-Gerrits et al., 2014). The high uncertainties of ET components partition hinder our understanding of ET subcomponents' authentic variation characteristics and their interactions in the carbon and water cycle of terrestrial ecosystems.

Several methods for partitioning T from ET have been used, including direct and indirect methods from the plot to the ecosystem scale (Kool et al., 2014; Stoy et al., 2019). At the plot scale, these mainly include the sap flow method, the gas-exchange chambers method, the micro-lysimeter method, and the isotopic method (Sun et al., 2019). These approaches can only determine the T/ET within a limited range and would create considerable uncertainty when extrapolating to ecosystem scale (Kool et al., 2014). Ways for partitioning E and T at the ecosystem scale generally combine ecosystem-scale observations with satellite-based algorithms, which can upscale E and T from ecosystem scale to regional or global scale. These approaches include empirical models based on the relationship between LAI and T/ET (Wang et al., 2014; Wei et al., 2017), thermal imaging (Marshall et al., 2016), water-use efficiency (WUE) combined with optimality theory assumption (plants minimize water loss per unit carbon dioxide (CO_2) gain) (Nelson et al., 2018; Scott and Biederman, 2017; Zhou et al., 2016), flux variance similarity (Scanlon and Kustas, 2010), and conditional eddy-covariance method (Zahn et al., 2022). The first two methods that use leaf attributes of the ecosystem from satellite observations, can capture the trend of T/ET over all ecosystems. Nevertheless, there are still significant variations in T/ET among ecosystems when leaf attributes are comparable (Sun et al., 2019). The latter two methods, which rely on plant carbon–water coupling characteristics, can precisely partition T from ET across all ecosystems. However, they require a reliable estimation of vegetation productivity (GPP) or canopy conductance (g_c), especially when applied at the regional or global scales in conjunction with remote sensing techniques (Nelson et al., 2020).

Remote sensing approaches have also been widely used in global ET estimation (Wang and Dickinson 2012). These approaches mainly contain (1) surface energy balance (SEB) based method, including single-source SEB model and dual-source SEB model, such as the operational Simplified Surface Energy Balance (SSEBop) developed by Senay et al. (2013); (2) water balance (WB) based method, including surface water balance and atmospheric water balance, such as the WB with Model Tree Ensemble (WB-MTE) developed by Zeng et al. (2014); (3) Penman-Monteith (PM) method, such as the Moderate Resolution Imaging Spectroradiometer (MODIS) ET product (PM-MOD) developed by Mu et al. (2011) and the Penman-Monteith-Leuning model (PML and PML-V2) developed by Zhang et al. (2016b, 2019b); (4) Priestley-Taylor (PT) method, such as the Global Land Evaporation Amsterdam Model (GLEAM) developed by Martens et al. (2017); (5) Surface temperature-vegetation index space (Ts-VI) method, such as the Surface Energy Balance System (SEBS) developed by Su (2002); (6) maximum entropy production method (MEP) applied to global estimation by Huang et al. (2017); (7) empirical or machine learning (EML) method, such as the Gridded FLUXNET ET with Model Tree Ensemble (GFET-MTE) developed by Jung et al. (2010); and (8) Assimilation method, such as the North American Land Data Assimilation System (NLDAS) developed by Xia et al. (2012). The common disadvantage of SEB, WB, Ts-VI, and MEP is only available for clear-sky. The drawbacks of WB include its inability to compute gridded ET values directly and its poor spatiotemporal resolution. The simplification of physical processes is a restriction shared by both PT and EML. PM can overcome these flaws, after acquiring high-quality meteorological forcing and improving the g_c estimate (Zhang et al., 2016a). However, g_c is closely coupled with photosynthesis, and improving estimations of g_c needs optimizing GPP modelling.

Spaceborne solar-induced chlorophyll fluorescence (SIF) has emerged as an essential technique for optimizing GPP estimation (Joiner et al., 2011; Li et al., 2018; Sun et al., 2017). Satellite sensors used for SIF retrieval in terrestrial vegetation include the Meteorological Operational satellite - Global Ozone Monitoring Experiment-2 sensor; the Orbiting Carbon Observatory; the Sentinel-5 Precursor - TROPOspheric Monitoring Instrument (TROPOMI); and other sensors (Mohammed et al., 2019). TROPOMI observations offer an excellent spatial and temporal resolution, which improves global estimates of GPP over previous satellite SIF data (Zhang et al., 2019c). SIF has been used to estimate g_c and T because it has a tight physical relationship with GPP (Damm et al., 2018; Lu et al., 2018; Maes et al., 2020; Pagan et al., 2019; Shan et al., 2019). The SIF-T connection is dominated by air temperature and intrinsic WUE (Maes et al., 2020) and also is affected by Photosynthetically Active Radiation (PAR), Vapor Pressure Deficit (VPD), and LAI (Lu et al., 2018). Moreover, SIF-based T retrieval models, including a WUE-based model and a conductance-based model, have been constructed from the standpoint of plant physiology (Feng et al., 2021; Shan et al., 2021). These SIF-based models perform well at the site scale. However, these SIF-based models are challenged to apply for quantifying T/ET and to employ in different ecosystems on the global scale.

The main objective of this study is to quantify T/ET on the global scale by using the SIF-constrained g_c model. Specifically, we aim to: (1) develop a plant functional type (PFT) specific SIF-driven semi-mechanism g_c model (denoted as g_c-SIF model); (2) partition ET across different PFTs worldwide combing the PM equation and SIF-constrained g_c; (3) apply the g_c-SIF model to global T estimation in the 2018 growing season.

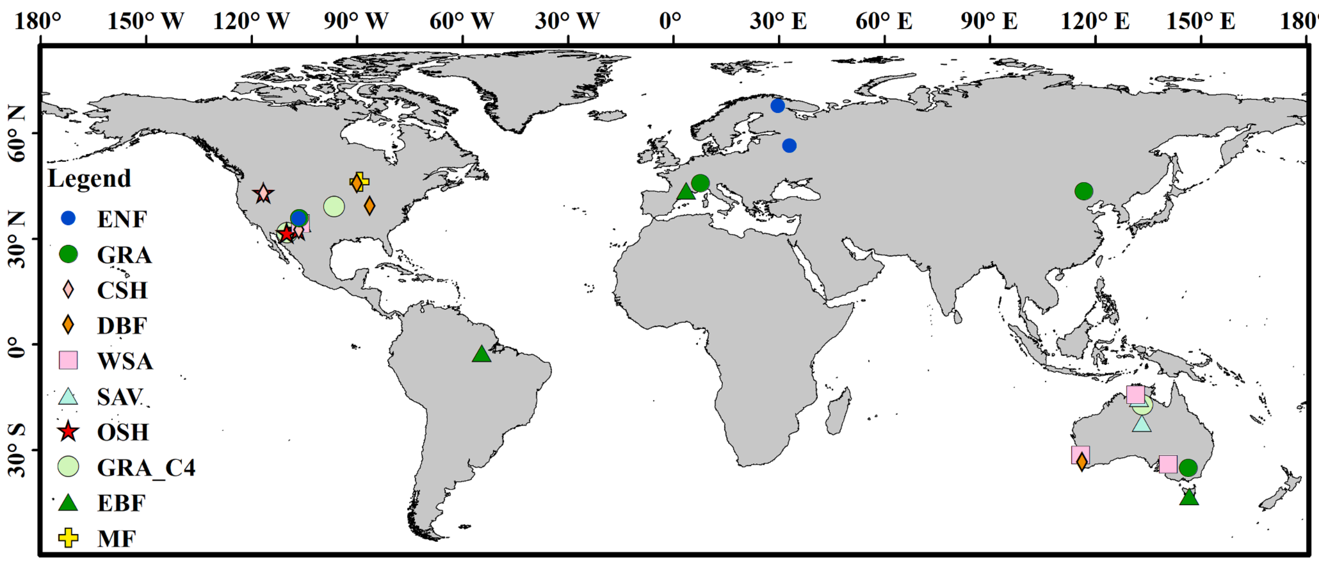

Fig. 2. The distribution of flux sites in this study.

2. Materials and methods

2.1. Workflow

First, we calculated g_c at 30 eddy-covariance (EC) flux tower sites using the Ball-Berry-Leuning (BBL) model (denoted as g_{cSITE}) covering ten different PFTs (see 2.3.1 for details). Second, g_{cSITE} was used to calculate and validate the g_c-SIF model and simulate g_c based on TROPOMI SIF data (denoted as g_{cSIF}) (see 2.3.2 for details). Third, g_{cSITE} and g_{cSIF} combined with the optimized PM model (PM_{opt}) were used to calculate T (denoted as T_{SITE} and T_{SIF}, respectively) for all sites (see 2.3.3 for details). Fourth, the results of T_{SIF} and T_{SIF}/ET were compared to previous studies at the ecosystem scale and on the global scale (see 2.3.4 for details). Fifth, a global and spatial estimation of terrestrial T was obtained using the g_c-SIF model and the PM_{opt} as well as SIF and other relevant data at a 16-day temporal resolution, represented as daily global T estimation. Finally, the global T estimates were compared to current state-of-the-art T estimates such as GLEAM and PML-V2. A detailed flowchart for data processing is shown in Fig. 1.

2.2. Dataset

2.2.1. Far-red SIF data from TROPOMI

SIF from the Sentinel 5 Precursor satellite was retrieved by using a singular value decomposition technique in the window of 743 ~ 758 nm and normalized to the SIF at 740 nm (Köhler et al., 2018). It was almost daily continuous global coverage with a spatial resolution of 7 km × 3.5 km at the nadir and 7 km × 14.5 km at the edge of the swath. It was available from February 2018, and our study period ran from February 2018 to July 2019. To avoid cloud impacts, we first filtered out the original SIF with cloud fractions>0.2. Second, the instantaneous SIF was transformed to daily means using the day-length correction factor before our investigation (Frankenberg et al., 2011). The daily mean SIF for each site was determined as the average of all available observations within a 10 km radius buffer centered by the site location, which can well capture the footprint of EC flux (Fig. A1). The ungridded daily mean SIF was aggregated to 0.1° × 0.1° gridded daily SIF data to estimate global T during the 2018 growing season. The 16-day SIF was further aggregated by averaging daily mean SIF (ungridded and gridded) over the 16 days when data was available for at least five days.

2.2.2. EC flux dataset

We collected a total of 30 EC flux sites after checking the availability of data to match the period of SIF distributed over America, Europe, Australia and China (Fig. 2 and Table A1), and all these sites have data records covering at least one entire growing season from February 2018 to July 2019. The growing season was defined as the five consecutive months with the highest ecosystem productivity in a year, as determined by a multi-year average of the recent five years. The 30 flux sites contain 10 different PFTs, comprising 3 evergreen needle forests (ENF) sites, 3 evergreen broadleaf forests (EBF) sites, 3 deciduous broadleaf forests (DBF) sites, 1 mixed forest (MF) site, 3 closed shrublands (CSH) sites, 4 open shrublands (OSH) sites, 3 woody savannas (WSA) sites, 3 savannas (SAV) sites, 4 C3 grasslands (GRA) sites, 3 C4 grasslands (GRA_{C4}) sites.

Flux data and relevant auxiliary data were available at AmeriFlux (https://ameriflux.lbl.gov), European Eddy Fluxes Database Cluster (https://www.europe-fluxdata.eu/), OzFlux (https://data.ozflux.org.au/) and few collaborating researchers. Flux data included net ecosystem exchange flux (unit: μmol m^{-2} s^{-1}), latent heat flux (LE, unit: W m^{-2}), and ground heat flux (G) (or sensible heat flux) (unit: W m^{-2}). Auxiliary data contained net radiation (R_n, unit: W m^{-2}), surface pressure (P, unit: kPa), 2 m temperature (T_{air}, unit: °C), soil temperature (unit: °C), CO_2 concentration ([CO_2], unit: parts per million, ppm), friction velocity (u*, unit: m s^{-1}), wind speed (u, unit: m s^{-1}), canopy height (h_c, unit: m), measurement height (h_m, unit: m), and air relative humidity (RH, unitless). If R_n was not directly available, R_n was calculated by the following formula:

$$R_n = R_{ns} + R_{nl} = R_s\downarrow - R_s\uparrow + R_l\downarrow - R_l\uparrow \tag{1}$$

where R_{ns}, R_{nl}, $R_s\downarrow$, $R_s\uparrow$, $R_l\downarrow$, $R_l\uparrow$ were surface net solar radiation, surface net thermal radiation, downward solar radiation, upward solar radiation, downward thermal radiation, and upward thermal radiation in W m^{-2}, respectively. VPD could substitute for RH, because RH and T_{air} were used to compute VPD by Tetens's formula:

$$VPD = e_{sat} \times (1 - RH) \tag{2}$$

$$e_{sat} = 0.61078 \times e^{\left(\frac{17.27 \times T_{air}}{T_{air}+237.3}\right)} \tag{3}$$

where VPD was in kPa, and e_{sat} is saturated vapour pressure in kPa.

The following processes aimed to make a rigorous quality check to identify reliable half-hour flux observations. First, a standard processing was carried out for the original flux data, including u* filtering, gap filling, and flux partitioning (Wutzler et al. 2018). Specifically, a daytime carbon flux partitioning algorithm was used for calculating GPP

Table 1
The empirical parameters used in the BBL model.

Type	m	g_0	Reference
GRA_{C4}	4	0.04	Ran et al. (2017)
BF (EBF & DBF)	12	0.01	Sprintsin et al. (2012)
ENF	10	0.01	Sprintsin et al. (2012)
OSH	8	0.0011	Chen et al. (2012)
CSH	9	0.01	Ran et al. (2017)
GRA	9	0.01	Ran et al. (2017)
SAV	9	0.01	Ran et al. (2017)
WSA	9	0.01	Ran et al. (2017)
MF	11	0.01	Average of BF and ENF

(Lasslop et al., 2010). Second, measured data without gap-filling was employed in this study except for standard processing of flux data. Third, half-hourly data were averaged into hourly data to standardize the calculation process. Fourth, observations with negative R_n, GPP, LE, and VPD were eliminated. Fifth, we used day-time observations from 6:00 to 18:00. Data availability after quality control is given in Table A2 at each site. In this study, daily values were computed only for days with at least 8 measured hour measurements, and 16-day values were calculated only for the 16-days with at least 3 recorded day measurements.

2.2.3. ERA5-Land data

For the global T estimation, we used the fifth European Centre for Medium-Range Weather Forecasts (ECMWF) ReAnalysis for land (hourly dataset ERA5-Land) as auxiliary data, which is the latest global land-surface climate reanalysis dataset with $0.1^\circ \times 0.1^\circ$ resolution (ECMWF, 2017). The uncertainty of ERA5-Land was defined by the ensemble of data assimilations system, which confirms that the data was reliable from February 2018 to July 2019. The hourly ERA5-Land variables used in this study included T_{air} (unit: K), 2 m dewpoint temperature (T_{dew}, unit: K), R_{ns} (unit: J m^{-2}), R_{nl} (unit: J m^{-2}), and P (unit: Pa). The units of all variables were converted to be consistent with the site flux dataset. The T_{dew} was used to calculate the VPD in kPa by the following equation:

$$RH = \frac{e_{sat,dew}}{e_{sat}} \tag{4}$$

$$VPD = e_{sat} \times \left(1 - \frac{e_{sat,dew}}{e_{sat}}\right) = e^{\left(\frac{17.27 \times T_{air}}{T_{air}+237.3}\right)} - e^{\left(\frac{17.27 \times T_{dew}}{T_{dew}+237.3}\right)} \tag{5}$$

where $e_{sat,dew}$ is the saturated vapor pressure at dew point temperature in kPa. R_n was calculated by the Eq. (1). Data with negative R_n and VPD was excluded. The hourly data was aggregated to daily data by averaging day-time data from 6:00 to 18:00.

2.2.4. MODIS data

MODIS data were obtained from google earth engine (GEE) MODIS collection 6 products from February 2018 to July 2019. The MCD15A3H.006 LAI and fPAR (i.e., fraction of PAR absorbed by vegetation) dataset (Myneni et al., 2015), have a spatial resolution of 500 m and a temporal resolution of 4-day, which were used to calculate g_{cSITE}. The MCD12Q1.006 land cover dataset at 500-m spatial resolution is annual land cover types (Friedl et al., 2010), and the year 2018 was used in this study. The international geosphere-biosphere programme classification scheme was used to provide PFT-specific information. The MOD16A2.006 ET dataset in 2018 was applied to magnify T/ET from PFT to global (Mu et al., 2011).

A Savitzky-Golay filter was utilized for each pixel to eliminate noise contaminations for LAI and fPAR data (Savitzky and Golay, 1964). The quality control was checked using the quality assurance layer, and pixels not contaminated by clouds and aerosols were selected as reliable observations. The LAI and fPAR around each flux tower site were extracted by averaging all available observations within a 1 km radius around the site location. To estimate T for different PFTs, the land cover data was aggregated to $0.1^\circ \times 0.1^\circ$ resolution by counting the proportions of different land cover types in each grid from the original 500 m resolution, and the dominant biome type was assigned to this $0.1^\circ \times 0.1^\circ$grid cell. Similarly, the LAI and fPAR datasets were also aggregated to $0.1^\circ \times 0.1^\circ$ resolution to keep the spatial resolution consistent with all other datasets.

2.2.5. GLEAM data and PML-V2 data

GLEAM and PML-V2 are widely-used remote sensed products of ET retrieved by PT and PM, which have dataset of different ET components. When this study is in progress, GLEAM and PML-V2 are available from 2018 to 2019. Thus, the GLEAM v3.3b data (Miralles et al., 2011; Martens et al. 2017) and the PML-V2 data (Zhang et al., 2019a) were compared to validate our estimation of T in this study. The daily GLEAM data was available from https://www.gleam.eu/, and provided on a $0.25^\circ \times 0.25^\circ$ latitude-longitude grid. The PML-V2 data was collected from GEE with a spatial resolution of 500 m and a temporal resolution of 8-day. The GLEAM data of each flux tower site was directly extracted by its location. The PML-V2 data of each flux tower site was extracted by the same strategies as MODIS LAI data. The GLEAM data were linearly interpolated to $0.1^\circ \times 0.1^\circ$ resolution, and the PML-V2 data were averagely aggregated to $0.1^\circ \times 0.1^\circ$ resolution to compare their spatial patterns with our results.

2.3. Methods

2.3.1. G_c estimation

We used the BBL model, a modified version of the Ball-Berry model, to estimate hourly leaf g_s. And then g_c was obtained within a big leaf model framework (Sellers et al., 1992). The BBL model is a biochemical model characterizing plants carbon–water coupling processes, in which g_s is expressed as a function of environmental parameters and net assimilation rate (A_n) (Leuning, 1995; Lohammer et al., 1980). The BBL model was given as follows:

$$g_s = 1.6 \times \left[\frac{m \times A_n}{(C_s - \Gamma) \times (1 + D_s/D_0)} + g_0\right] \tag{6}$$

where g_s was in unit of m s^{-1} or mol m^{-2} s^{-1}, A_n was in unit of μmol m^{-2} s^{-1}, C_s was [CO_2] at the leaf surface (ppm), Γ was the CO_2 compensation point (ppm), which was set to 40 for C3 plants and 2 for C4 grassland, D_s was humidity deficit at the leaf surface (kPa), D_0, was set to 0.35 as an empirically fitted parameter representing the sensitivity of stomata to changes in D_s (kPa) (Leuning, 1995). m and g_0 were the slope and minimum conductance calculated from empirical data provided in Table 1, respectively. The unit of g_s was converted from mol m^{-2} s^{-1} to m s^{-1} after a multiplication of the coefficient V_m. V_m was calculated according to the following equation:

$$V_m = \frac{8.314 \times (T_{air} + 273.15)}{1000 \times P} \tag{7}$$

Finally, we replaced g_0 with a multiplication of LAI and g_0, GPP with A_n, atmosphere [CO_2] with C_s, and VPD with D_s, to upscale all parameters from leaf to canopy scale. Different g_c models have little influence on the results of g_c after we compared the daily mean stomatal conductance calculated by the BBL model and the Ball-Berry-Medlyn model (BBM, Fig. A2, Lin et al., 2015; Medlyn et al., 2011).

2.3.2. The g_c-SIF model development and calibration

Shan et al. (2021) developed a SIF-driven semi-mechanism g_c model combining theories on the photosynthetic pathway and optimal stomatal behavior and validated by hourly canopy SIF and concurrent eddy covariance flux observations at both forest and crop ecosystems. The form of this model was expressed as follows:

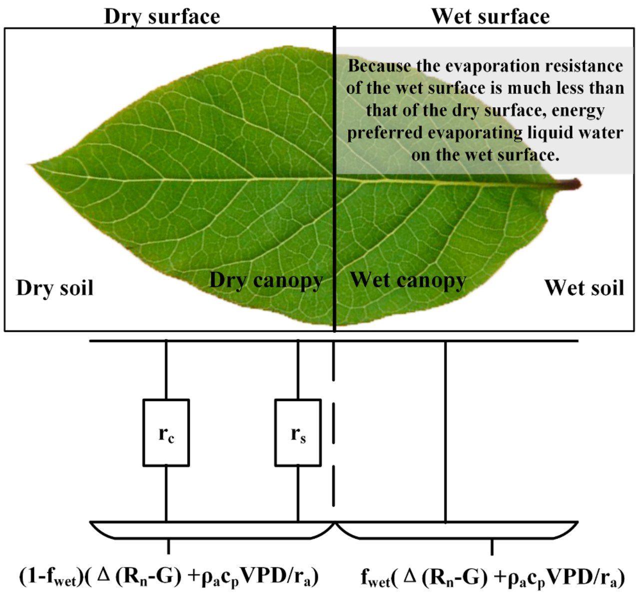

Fig. 3. Schematic plot of ET energy distribution in PM_{opt} equation.

Table 2
Model parameters and validation results of the g_c-SIF model.

Type	Model Slope	Model Intercept	RMSE, m s^{-1} $Pa^{0.5}$	MAE, m s^{-1} $Pa^{0.5}$	R^2
GRA_{C4}	0.0291	0.0015	0.0024	0.0019	0.88
GRA	0.0172	0.0026	0.0027	0.0023	0.50
OSH	0.0095	0.0014	0.0008	0.0007	0.41
SAV	0.023	0.0041	0.0015	0.0014	0.80
CSH	0.0361	0.0023	0.0025	0.0022	0.7
WSA	0.0223	0.0053	0.0024	0.0020	0.75
ENF + MF	0.0324	0.0042	0.0034	0.0030	0.81
DBF + EBF	0.0254	0.0077	0.0062	0.0051	0.73

$$g_c = VPD^{-0.5} \times (a \times SIF + b) \tag{8}$$

where SIF was in mW m^{-2} nm^{-1} sr^{-1}, *a* and *b* were the slope and intercept, which provided the constraint for the relationships between g_c and SIF for each PFT. We extended this model to 10 different PFTs worldwide using least squares regression and repeated K-Fold cross-validation at the 16-day temporal resolution. We repeated 4 times K-Fold cross-validation for each PFT, with K value of 10. The results for each PFT, including model slope, model intercept, mean square error (MSE), root mean square error (RMSE), mean absolute error (MAE), and goodness of fit (R^2), were computed by averaging the results of all the repeated K-Fold cross-validation.

2.3.3. Transpiration estimation

The PM equation was used to estimate T. The original PM equation and relevant formulas were as follows:

$$LE = \frac{\Delta \times (R_n - G) + \rho_a \times c_p \times VPD/r_a}{\Delta + \gamma \times (1 + r_s/r_a)} \tag{9}$$

$$\Delta = 4098.17 \times e_{sat}/(T_{air} + 237.3)^2 \tag{10}$$

$$\rho_a = \frac{28.9654 \times (P - e_{sat,dew}) + 18.016 \times e_{sat,dew}}{8.314 \times (273.15 + T_{air})} \tag{11}$$

$$c_p = 1005 \times \left(1 - 0.622 \times \frac{e_{sat,dew}}{P}\right) + 1820 \times \frac{e_{sat,dew}}{P} \tag{12}$$

$$\gamma = \frac{c_p \times P}{0.622 \times (-2.2 \times T_{air} + 2500)} \tag{13}$$

$$r_a = \frac{ln\left(\frac{h_m - 2\times h_c/3}{0.123\times h_c}\right) \times ln\left(\frac{h_m - 2\times h_c/3}{0.0123\times h_c}\right)}{k^2 \times u} \tag{14}$$

$$r_s = \frac{1}{G_s} \tag{15}$$

where *LE* was in W m^{-2}, Δ was the slope of the saturation vapour pressure temperature relationship in kPa °C^{-1}, ρ_a was the mean air density at constant pressure in kg m^{-3}, c_p was the specific heat of the air in J kg^{-1} °C^{-1}, r_a was the aerodynamic resistance in s m^{-1}, γ is the psychrometric constant in kPa °C^{-1}, r_s was the surface resistance in s m^{-1}, and G_s was the surface conductance in m s^{-1} or mol m^{-2} s^{-1}. The PM equation was originally used to calculate ET, and was modified to determine T after considering energy distribution between dry and wet surfaces. Energy preferred evaporating liquid water on the wet surface, similar to the parallel circuit system, since the evaporation resistance of the wet surface was considerably lower than that of dry surface, as illustrated in Fig. 3. Moreover, G_s had to be substituted with g_c while calculating T. As a result, the PM_{opt} equation for calculating T was as follows:

$$\lambda T = (1 - f_{wet}) \times \frac{\Delta \times (R_n - G) + \rho_a \times c_p \times VPD/r_a}{\Delta + \gamma \times [1 + 1/(g_c \times r_a)]} \tag{16}$$

$$f_{wet} = \begin{cases} 0.0RH < 70\% \\ RH^4 70\% \leq RH \leq 100\% \end{cases} \tag{17}$$

where λT was the latent heat flux from T in W m^{-2}, λ was the latent heat of vaporization, 2.45 MJ kg^{-1}, f_{wet} was the wet surface fraction from the Fisher et al. (2008) ET model (Fisher et al., 2008).

All abbreviations are listed in Supplemental Table B1.

2.3.4. Comparison with previous T/ET estimations

First, T/ET estimated from both the BBL model and the g_c-SIF model were evaluated using the Pearson correlation analysis at the site scale. Second, we used correlation analysis to examine the relationship between our T_{SIF}/ET finding and prior multi-site T/ET results (collected by Wei et al. (2017)). Wei et al. (2017) collected the values of T, E, I, ET, and PFT type from 64 individual ground sties. Since these ground sites are different from the sites in our study, we can only compare our results with Wei's results at PFT scale. Third, to further explore the performance of our gc-SIF model, we estimated the global mean T_{SIF}/ET of terrestrial ecosystem for the 2018 growing season using T_{SIF}/ET values at the PFT scale and the method from Schlesinger and Jasechko (2014) combined with MODIS ecozone ET (Mu et al., 2011) and land cover product (Friedl et al., 2010, Table 3). Finally, we compared our global T_{SIF}/ET result to T/ET values using other methodologies reported in the previous literature.

3. Results

3.1. Calibration and validation of the g_c-SIF model

We first examined the relationship between SIF and both GPP and $g_{cSITE} \times VPD^{0.5}$ for all sites over the growing season at both daily and 16-day temporal scale (Fig. 4). In general, the linear relationship can be observed between daily SIF and GPP with R^2 of 0.50 (Fig. 4a). The SIF-GPP relationship presents an increasing linearity and an improvement after aggregating from daily to 16-days (R^2 increased to 0.56, Fig. 4b). For the majority of sites, SIF shows significantly positive correlations with GPP ($p < 0.05$, 21 out of 30 sites) at the 16-day temporal scale (Table A3), and the mean site-based R between SIF and GPP is 0.62. The correlation between $g_{cSITE} \times VPD^{0.5}$ and SIF is less scattered and more

Table 3
Statistics of the global mean T/ET calculated by different methods.

Year	Method	Type of method	T/ET	SD
2005	Gerten et al., LPJ	Climate model	0.65	0.03
2006	Dirmeyer et al., GSWP-2	Climate model	0.48	0.03
2007	Lawrence et al., CLM3	Climate model	0.44	
2009	Alton et al., JULES	Climate model	0.38	0.09
2010	Cao et al., CLM3.5/CAM3.5	Climate model	0.41	0.03
2011	Lawrence et al., CLM3.5	Climate model	0.43	
2011	Lawrence et al., CLM4CN	Climate model	0.56	
2011	Lawrence et al., CLM4CNE	Climate model	0.56	
2011	Lawrence et al., CLM4SP	Climate model	0.48	
2012	Ito and Inatomi, VISIT/Sim-CYCLE	Climate model	0.24	
2014	Wang-Erlandsson et al., STEAM	Climate model	0.59	
2016	Maxwell and Condon, ParFlow-CLM	Climate model	0.62	0.12
2017	Fatichi et al. T&C	Climate model	0.7	0.09
2017	Wei et al. CMIP5	Climate model	0.43	0.12
2018	Lian et al., CMIP5	Climate model	0.41	0.11
2018	Lian et al., CMIP5 constrained	Climate model	0.62	0.06
2018	Yang et al., CLM4.5	Climate model	0.48	
2006	Yoshimura et al., Iso-Matsiro	Isotope	0.31	
2013	Jasechko et al.	Isotope	0.86	0.07
2014	Coenders-Gerrits et al.	Isotope	0.58	0.33
2015	Good et al.	Isotope	0.64	0.13
2014	Wang et al.	LAI-Based model	0.6	0.3
2017	Wei et al.	LAI-Based model	0.57	0.07
2011	Compo et al., NOAA 20CR	Reanalysis Data	0.39	
1998	Choudhury and DiGirolamo	Remote sensing model	0.52	
2011	Miralles et al., GLEAM	Remote sensing model	0.8	
2016	Miralles et al., GLEAM	Remote sensing model	0.76	
2016	Miralles et al., PM-MOD	Remote sensing model	0.24	
2016	Miralles et al., PT-JPL	Remote sensing model	0.56	
2016	Zhang et al., PML	Remote sensing model	0.65	0.04
2019	Mianabadi et al., Gerrits's model	Remote sensing model	0.71	
2019	Mianabadi et al., GLEAM v3.0a	Remote sensing model	0.71	
2019	Zhang et al., PML-V2 (computed by this study)	Remote sensing model	0.55	0.07
2014	Schlesinger and Jasechko	Site statistics	0.61	0.15
2016	Zhou et al.	WUE-based model	0.57	0.04
2019	Li et al.	WUE-based model	0.66	0.15
now	This study, site level SIF model	Site statistics	0.57	0.14

linear compared with the SIF-GPP relationship, with an improved R^2 of 0.69 for daily scale (Fig. 4c) and R^2 of 0.76 for 16-day temporal scales (Fig. 4d) for all sites. At the individual site, 23 of 30 sites demonstrate significant ($p < 0.05$) associations between SIF and $g_{cSITE} \times VPD^{0.5}$ (Table A3). The mean site-based R between SIF and $g_{cSITE} \times VPD^{0.5}$ is 0.48. Most of these sites (12/19 sites) show a stronger linear correlation between SIF and $g_{cSITE} \times VPD^{0.5}$ than between SIF and GPP. In short, the relationship between SIF and $g_{cSITE} \times VPD^{0.5}$ at the 16-day scale is strongest among these four relationships.

We further explored the performance of the SIF-$g_{cSITE} \times VPD^{0.5}$ linear regressions at both daily and 16-day scales for each biome (Fig. 5). The regression models vary significantly across PFTs, and the R^2 ranges from 0.03 for OSH to 0.6 for GRA_{C4} at daily scale. The regressions show improved R^2 (R^2 ranges from 0.28 for OSH to 0.83 for GRA_{C4}) and increased magnitude in slopes across PFTs when aggregating daily to 16-day. Correlations between 16-day SIF and $g_{cSITE} \times VPD^{0.5}$ are generally high ($R > 0.75$) for GRA_{C4}, CSH, WSA, SAV, ENF + MF and DBF + EBF, but low ($0.75 > R > 0.5$) for GRA as well as OSH. According to the

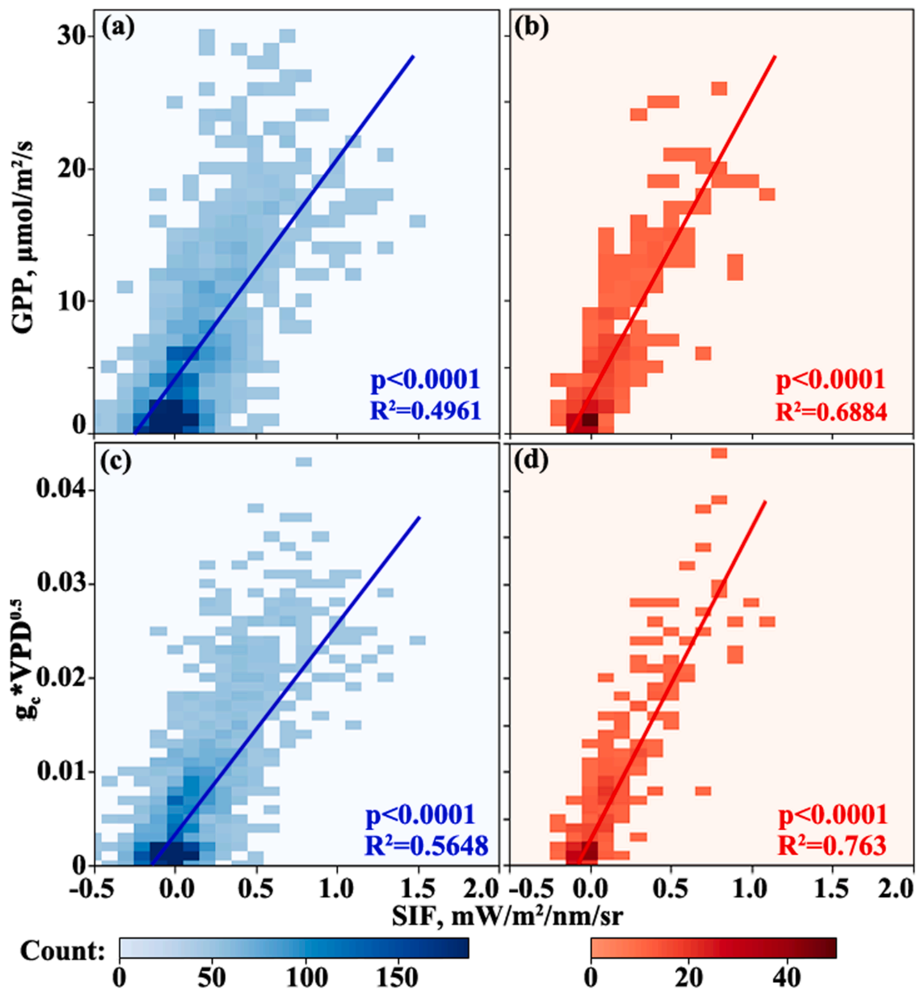

Fig. 4. The relationship between SIF and both GPP ((a) and (b)) and $g_c \times VPD^{0.5}$ ((c) and (d)) at all sites from daily ((a) and (c)) and 16-day ((b) and (d)) data. All R^2 are statistically significant ($p < 0.0001$).

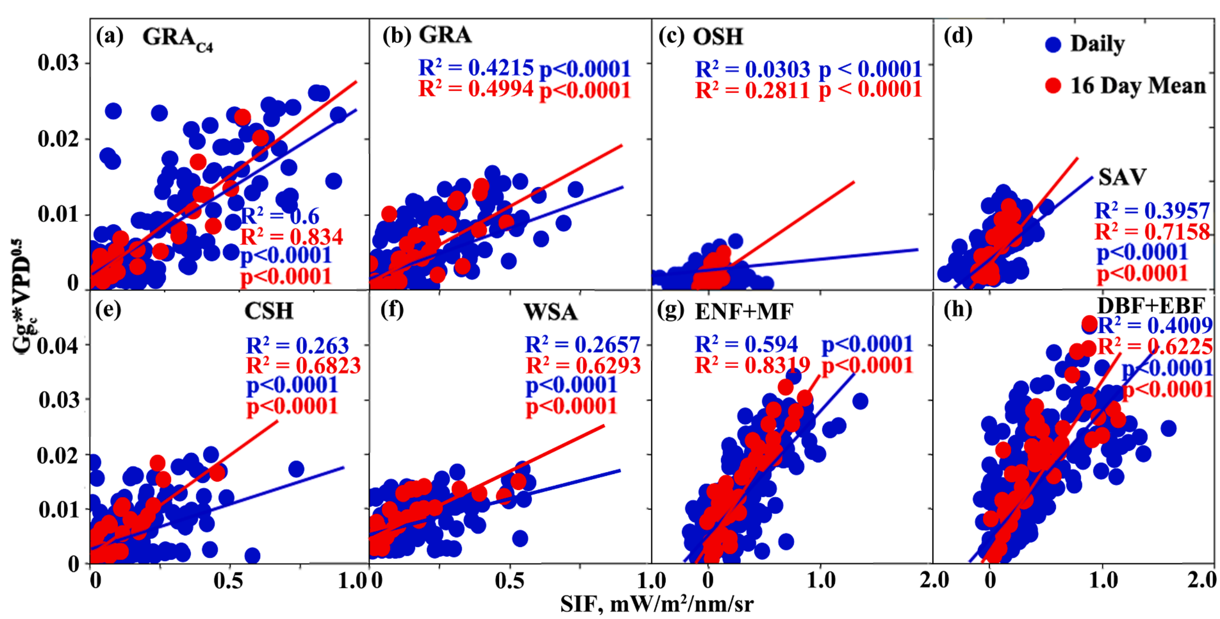

Fig. 5. The relationship between SIF and both GPP and $g_{cSITE} \times VPD^{0.5}$ per PFT from daily and 16-day data. R^2 is calculated by simple correlation analysis.

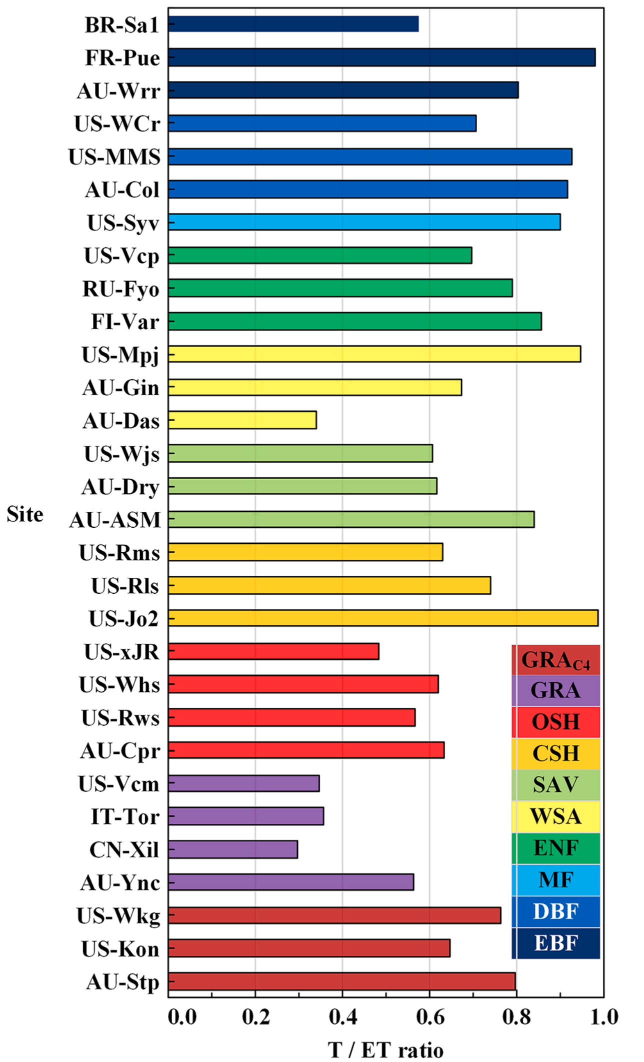

Fig. 6. The T_{SIF}/ET for each site calculated by the g_c-SIF model.

significant correlation between SIF and $g_{cSITE} \times VPD^{0.5}$, we calculated the slope and intercept per PFT in the g_c-SIF model (Table 2). The results show that the slopes of CSH and OSH are the greatest and lowest, respectively. The best performance of the model was observed for GRA_{C4} ($R^2 = 0.88$), while the worst was obtained for OSH ($R^2 = 0.41$). Similar to R^2 between SIF and $g_{cSITE} \times VPD^{0.5}$, the model slopes for GRA and OSH are lower than those for other PFTs. Finally, the values of *a* and *b* in the g_c-SIF model across different PFTs are obtained.

3.2. T/ET Comparation

T_{SIF}/ET at the site scale was calculated using the simulated T_{SIF} and the observed ET (Fig. 6). T_{SIF}/ET ratio is the greatest for MF (0.90), which is limited to a single site. The lowest T_{SIF}/ET ratio is for GRA (0.39). DBF is the PFT with the second greatest T_{SIF}/ET (0.85). For individual sites, the FR-Pue EBF site has the highest T_{SIF}/ET (0.98) of all the sites, while the lowest T_{SIF}/ET value (0.30) is seen at the CN-Xil GRA site. Interestingly, for evergreen forests, ENF's mean T_{SIF}/ET (0.78) is close to that of EBF (0.78). Due to a high vegetation coverage for CSH, an average T_{SIF}/ET ratio of 0.78 is observed. The mean T_{SIF}/ET values in WSA, SAV and OSH, are 0.65, 0.69 and 0.57, respectively. Moreover, there is a substantial difference in the T_{SIF}/ET for C3 grasslands and C4 grasslands with different CO_2 assimilation pathways, with GRA_{C3} having a mean T_{SIF}/ET value of 0.39 and GRA_{C4} having a mean T_{SIF}/ET value of 0.73. Both the BBL model (Fig. A3) and the g_c-SIF model provide comparable T/ET values for PFTs, but the ranking of T_{SITE}/ET for PFTs with high vegetation coverage is not entirely consistent (MF > EBF > DBF > CSH > GRA_{C4} > ENF > WSA > SAV > OSH > GRA).

T_{SITE}/ET is highly correlated with T_{SIF}/ET ($R^2 = 0.69p < 0.001$ Fig. 7a). In addition, our T_{SIF}/ET values were further compared with the T/ET values from Wei et al. (2017) using data from earlier research (Fig. 7b). The R^2 between our PFT-mean T_{SIF}/ET values and PFT-mean T/ET from Wei et al. (2017) is 0.70, a significant correlation ($p = 0.037$). The R^2 for PFT-median value is 0.86 ($p = 0.08$). These two comparative studies demonstrate the potential of the g_c-SIF model in T_{SIF}/ET estimation across a wide variety of PFTs. GRA has the lowest mean and median T/ET values, while forests, including ENF, DBF and EBF (The last two are referred to BF.), have the highest mean and median T/ET values. SAV, WSA, and shrublands (OSH and CSH), all have mean and median T/ET values around 0.6 with a large standard deviation. But pattern of the mean T/ET values for SAV, WSA, and shrublands are different in our results than in Wei's results. In a word, our T_{SIF}/ET values are well validated by T_{SITE}/ET and T/ET from Wei et al. (2017).

To further explore the performance of our g_c-SIF model, we estimated the global mean T_{SIF}/ET of terrestrial ecosystem for the 2018 growing season using T_{SIF}/ET values at the PFT scale and the method from Schlesinger and Jasechko (2014) combined with MODIS ET and landcover product (Table 3). Our growing season global mean T_{SIF}/ET value is 0.57 ± 0.14. Global mean T/ET values calculated by different methods vary from 0.24 to 0.86, whereas our result falls within this range and close to their mean value. Global mean T/ET values computed

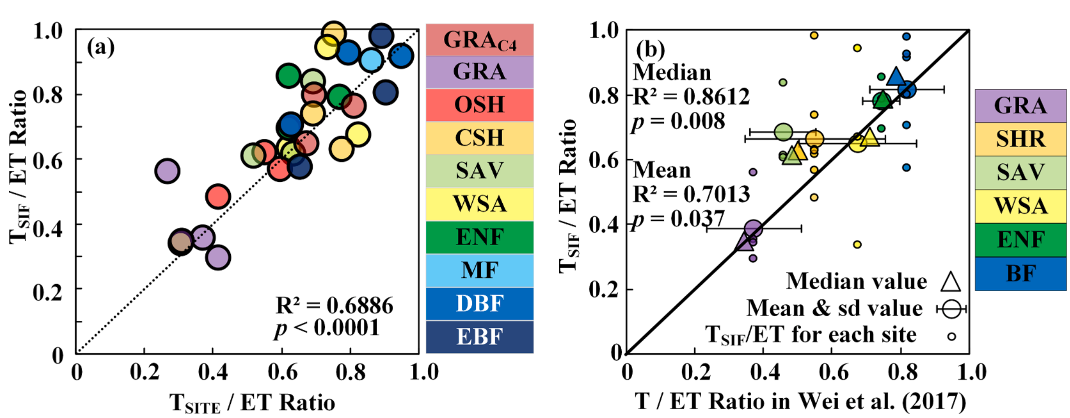

Fig. 7. (a) The correlation between T/ET calculated by the BBL model and by the g_c-SIF model at the site scale. (b) The correlation between T/ET selected by Wei et al. (2017) and calculated by the g_c-SIF model at the PFT scale. SHR is shrublands, including OSH and CSH. BF is broadleaf forests, including EBF and DBF. The small points in (b) represent the T_{SIF}/ET value of each site when the T/ET ratio in Wei et al. (2017) is the average value of each PFT.

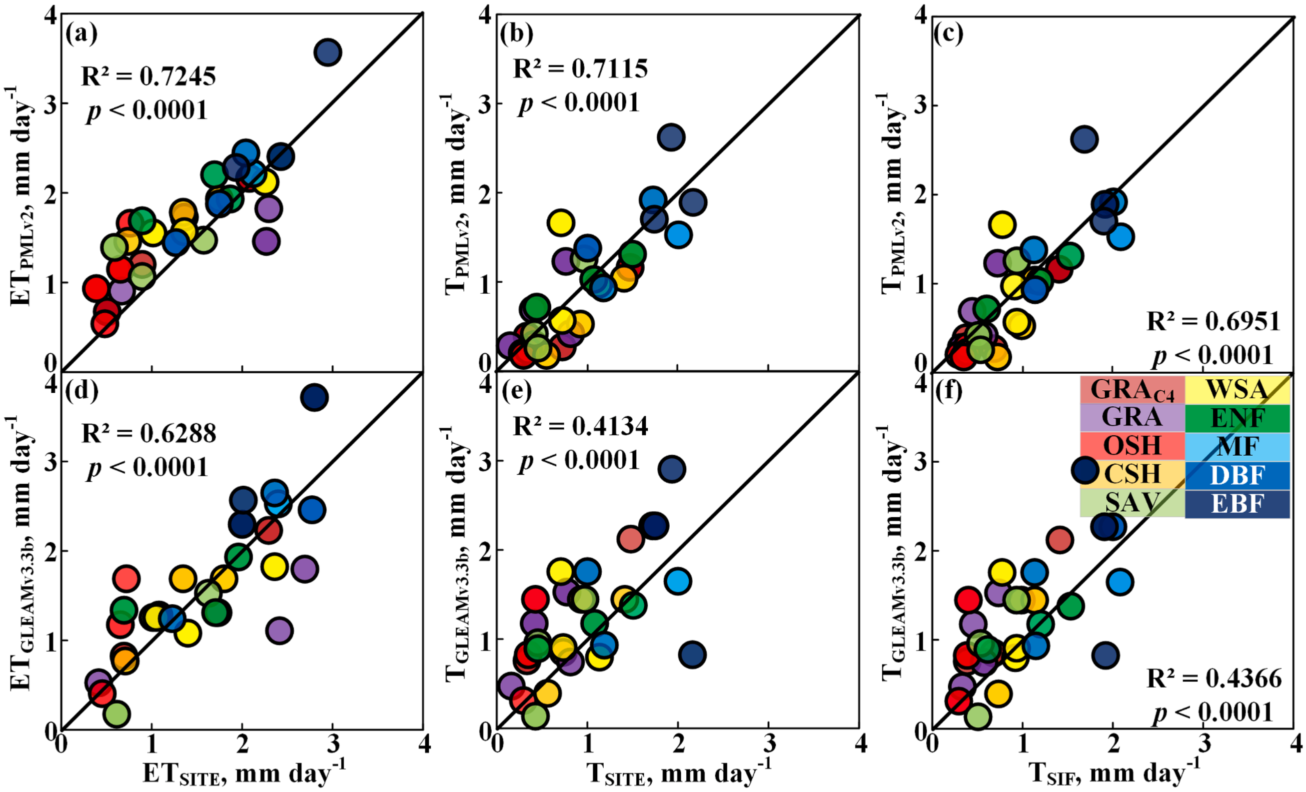

Fig. 8. Comparison of ET_{SITE}, T_{SITE} and T_{SIF} with GLEAM and PML-V2 products. ET_{SITE} is ET measured by flux tower. T_{SITE} is T calculated by the BBL model. T_{SIF} is T calculated by our g_c-SIF model.

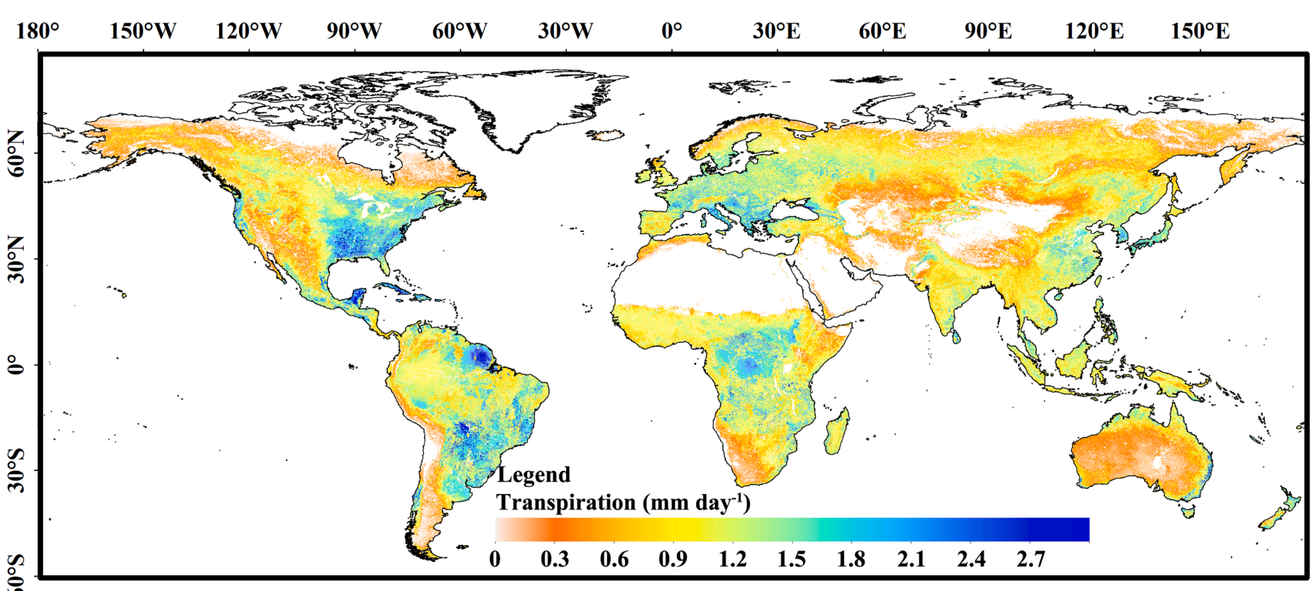

Fig. 9. The average daily T for the 2018 growing season worldwide calculated by our g_c-SIF model as well as ERA5-land data and MODIS data.

using climate models, isotopes, LAI-based models, remote sensing models, and WUE-based models are 0.50, 0.60, 0.59, 0.61, and 0.62. The uncertainties (measured as standard deviation, SD) also vary widely across models ranging from 0.03 to 0.33, while our global T_{SIF}/ET has an SD of 0.14. Moreover, we evaluated the global mean T/ET (0.55 ± 0.07) for 2018 using PML-V2 data. Thus, our growing season global mean T_{SIF}/ET value is comparable to the average of global mean T/ET values from other methods.

3.3. Global T estimation with the g_c-SIF model

Our T estimates based on the g_c-SIF model were compared to those from GLEAM and PML-V2 products at the site scale (Fig. 8). ET simulated by PML-V2 and GLEAM are strongly correlated with ET measured from EC flux tower, with the R values of 0.85 and 0.79. The correlations between the T from PML-V2 and both T_{SITE} and T_{SIF} are more significant than those between the ET from PML-V2 and the ET from the flux tower,

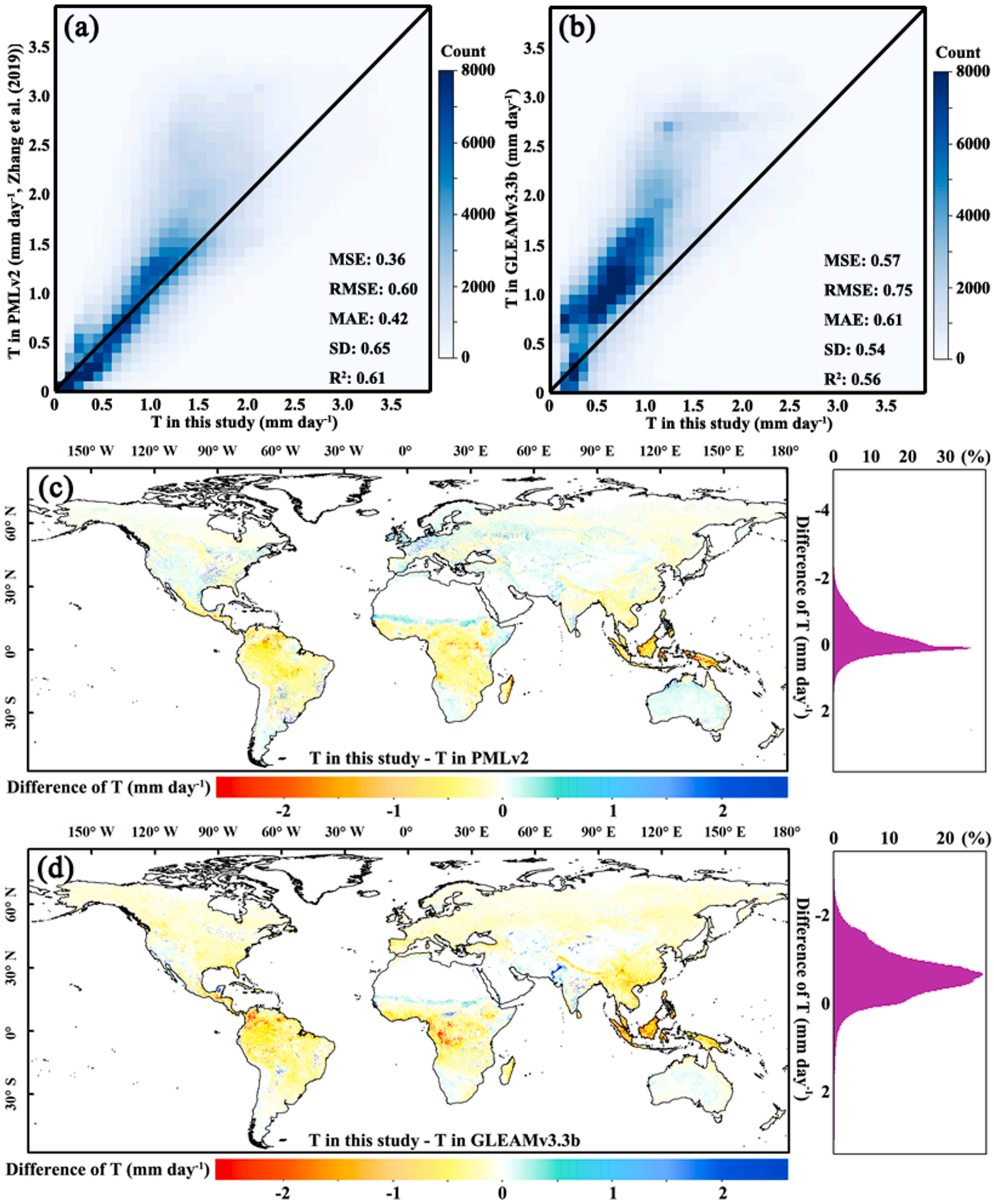

Fig. 10. The comparation of the global average daily T for the 2018 growing season between our result and both PML-V2 and GLEAM products.

while the correlations between the T from GLEAM and both T_{SITE} and T_{SIF} are less than those between the ET from GLEAM and the ET from the flux tower. Moreover, for most sites, the T estimated by GLEAM is higher than T_{SITE} and T_{SIF}.

The global spatial pattern of the average daily T_{SIF} for the 2018 growing season is shown in Fig. 9. The daily mean T_{SIF} value varies between 0 and 3 mm day^{-1} globally (Fig. 9). The growing season mean T_{SIF} shows the high values (T_{SIF} > 1.5 mm day-1) in the tropical rain forest area (including the Amazon basin and the Congo river basins) and the temperate broad-leaved forest area (including southeastern United States, southern Europe, and southern China). The intermediate T_{SIF} values range from 0.8 mm day^{-1} to 1.5 mm day^{-1} in the crop area (e.g., central United States, Sahel area, central and eastern Europe, south Asia, and eastern China) and the ENF area (e.g., southern Canada, northern Europe and northeastern China). The low values (T_{SIF} < 0.8 mm day^{-1}) are in the arid and semi-arid areas, as well as the areas with high latitude and altitude, which are characterized by sparse vegetation.

Our global T_{SIF} mapping can exhibit the spatial pattern of terrestrial ecosystem T globally, which is consistent with the current global T estimates. This consistency is simultaneously confirmed by the strong

Table A1

The basic information of FLUXNET sites used in this study. Characteristics of the sites include latitude (in degree), longitude (in degree), h_m (measurement height, in meters), h_c (canopy height, in meters), and international geosphere-biosphere programme (IGBP) plant functional type (PFT). EBF is evergreen broadleaf forests, ENF is evergreen needleleaf forests, DBF is deciduous broadleaf forests, MF is mixed forests, CSH is closed shrublands, OSH is open shrublands, WSA is woody savannas, SAV is savannas, GRA is C3 grasslands, and GRA_{C4} is C4 grasslands.

Site	No.	PFT	Name	Latitude	Longitude	h_m	h_c
AU-ASM	1	SAV	Alice Springs	−22.2828	133.2493	11.6	6.5
AU-Col	2	DBF	Collie	−33.4200	116.2370	35	10
AU-Cpr	3	OSH	Calperum	−34.0027	140.5877	10	2
AU-Das	4	WSA	Daly River Cleared	−14.1592	131.3881	23	16.4
AU-Dry	5	SAV	Dry River	−15.2588	132.3706	15	12.3
AU-Gin	6	WSA	Gingin	−31.3764	115.7139	14.8	6.8
AU-Stp	7	GRA_{C4}	Sturt Plains	−17.1507	133.3502	4.8	1.2
AU-Wrr	8	EBF	Warra	−43.0950	146.6545	81	55
AU-Ync	9	GRA	Australia Yanco site	−34.9893	146.2907	8	1.2
BR-Sa1	10	EBF	Santarem-Km67-Primary Forest	−2.85667	−54.95889	57.8	50
CN-Xil	11	GRA	Xilinhot	43.5500	116.6667	5	1.2
FI-Var	12	ENF	Varrio	67.7549	29.6100	16.6	8.61
FR-Pue	13	EBF	Puechabon	43.7413	3.5957	12.2	7
IT-Tor	14	GRA	Torgnon	45.8444	7.5781	2.5	0.5
RU-Fyo	15	ENF	Fyodorovskoye	56.4615	32.9221	31	17
US-Jo2	16	CSH	Jornada Experimental Range Mixed Shrubland	32.5849	−106.6032	7.1	1
US-Kon	17	GRA_{C4}	Konza Prairie LTER (KNZ)	39.0824	−96.5603	3	0.5
US-MMS	18	DBF	Morgan Monroe State Forest	39.3200	−86.4100	46	32.2
US-Mpj	19	WSA	Mountainair Pinyon-Juniper Woodland	34.4385	−106.2377	9.33	5
US-Rls	20	CSH	RCEW Low Sagebrush	43.1439	−116.7356	2.09	0.6
US-Rms	21	CSH	RCEW Mountain Big Sagebrush	43.0645	−116.7486	2.5	1.2
US-Rws	22	OSH	Reynolds Creek Wyoming big sagebrush	43.1675	−116.7132	2.05	0.6
US-Syv	23	MF	Sylvania Wilderness Area	46.2420	−89.3477	36	21.8
US-Vcm	24	GRA	Valles Caldera Mixed Conifer	35.8884	−106.5321	23.6	19.1
US-Vcp	25	ENF	Valles Caldera Ponderosa Pine	35.8642	−106.5967	23.8	21
US-WCr	26	DBF	Willow Creek	45.8059	−90.0799	29.6	18
US-Whs	27	OSH	Walnut Gulch Lucky Hills Shrub	31.7438	−110.0522	6.5	0.5
US-Wjs	28	SAV	Willard Juniper Savannah	34.4255	−105.8615	8	2
US-Wkg	29	GRA_{C4}	Walnut Gulch Kendall Grasslands	31.7365	−109.9419	6.4	0.3
US-xJR	30	OSH	NEON Jornada LTER (JORN)	32.5907	−106.8425	6.5	0.8

Table A2

The data availability after quality control at all sites.

Site ID	Site name	PFT	Number of hourly data
1	AU-ASM	SAV	1108
2	AU-Col	DBF	2297
3	AU-Cpr	OSH	3825
4	AU-Das	WSA	2291
5	AU-Dry	SAV	2427
6	AU-Gin	WSA	2782
7	AU-Stp	GRA_{C4}	1490
8	AU-Wrr	EBF	1054
9	AU-Ync	GRA	3299
10	BR-Sa1	EBF	1679
11	CN-Xil	GRA	1764
12	FI-Var	ENF	1804
13	FR-Pue	EBF	1693
14	IT-Tor	GRA	3228
15	RU-Fyo	ENF	3501
16	US-Jo2	CSH	1135
17	US-Kon	GRA_{C4}	1437
18	US-MMS	DBF	3052
19	US-Mpj	WSA	1837
20	US-Rls	CSH	1806
21	US-Rms	CSH	1781
22	US-Rws	OSH	933
23	US-Syv	MF	2818
24	US-Vcm	GRA	2427
25	US-Vcp	ENF	2316
26	US-WCr	DBF	3595
27	US-Whs	OSH	2891
28	US-Wjs	SAV	3512
29	US-Wkg	GRA_{C4}	765
30	US-xJR	OSH	2173

correlation with the PML-V2 product (R^2 = 0.61; RMSE = 0.60 mm day^{-1}) and the GLEAM product (R^2 = 0.56; RMSE = 0.75 mm day^{-1}) on a per pixel basis (Fig. 10). In most places, the magnitudes of T from GLEAM products are higher than our results. The T of PML-V2 product exceeds our findings only in the areas with high T intensity (T > 1.5 mm day^{-1}), mostly distributed in the tropics. In the arid and semi-arid areas, as well as some crop areas, the T of PML-V2 and GLEAM products is lower than our results.

4. Discussion

Accurate assessment of the contribution of T to ET is critical for understanding terrestrial ecosystem carbon and water cycle (Good et al., 2015; Wei et al., 2018). This study constructed a g_c-SIF model to simulate g_c and T based on satellite SIF data. The model is used to estimate the global mean T/ET and T values for the growing season of the year 2018.

4.1. *Influencing factors of partitioning T from ET based on SIF*

Our study shows that SIF links closely with GPP at different temporal scales (Fig. 4), consistent with previous findings (Guanter et al., 2014; Yang et al., 2015). The mechanic linkage between photosynthesis and SIF provides a valuable opportunity to estimate T, since GPP and T are coupled through stomatal function (Stoy et al., 2019). However, SIF cannot directly and exclusively estimate T, owing to the impact of confounding factors, such as micro-meteorological conditions, plant physiological characteristics, and canopy structure (Damm et al., 2018; Maes et al., 2020). A lucubration of the SIF-T relationship prompts researchers to develop two techniques for T retrieval via SIF, including the SIF-g_c empirical relationship-based model (Shan et al., 2019) and the mechanism model (Feng et al., 2021; Shan et al., 2021). We adopt the mechanism framework proposed by Shan et al. (2021) to connect SIF

Table A3
The correlations between SIF_{TRO} and both $g_c \times VPD^{0.5}$ and GPP at all sites. R^2 is the coefficient of determination. The count is the number of useful 16-day observations. R is the Pearson correlation coefficient. The red numbers in column R for $g_c \times VPD^{0.5}$ indicate that R for $g_c \times VPD^{0.5}$ is greater than R for GPP.

ID	Count	PFT	R for GPP	p value for GPP	R for $g_c \times VPD^{0.5}$	p-value for $g_c \times VPD^{0.5}$
1	3	SAV	-0.3183	>0.05	-0.8535	<0.05
2	28	DBF	-0.5499	<0.05	0.0024	>0.05
3	32	OSH	-0.5223	<0.05	-0.4066	<0.05
4	20	WSA	0.4238	<0.05	0.9281	<0.01
5	23	SAV	0.178	>0.05	0.5255	<0.05
6	29	WSA	0.1778	>0.05	0.1546	>0.05
7	25	GRA_{C4}	0.9963	<0.01	0.8383	<0.01
8	6	EBF	-0.8648	<0.05	-0.8811	<0.01
9	33	GRA	0.9295	<0.01	0.9442	<0.01
10	18	EBF	0.6955	<0.01	-0.2214	>0.05
11	10	GRA	0.829	<0.01	0.8345	<0.01
12	14	ENF	0.907	>0.01	0.9272	<0.01
13	11	EBF	0.3516	<0.05	0.333	>0.05
14	16	GRA	0.5216	<0.01	0.5868	<0.05
15	30	ENF	0.8762	<0.01	0.8818	<0.01
16	15	CSH	0.5744	<0.01	0.06	>0.05
17	15	GRA_{C4}	0.8318	<0.01	0.8382	<0.01
18	32	DBF	0.8501	<0.01	0.8805	<0.01
19	12	WSA	0.6981	<0.05	0.7089	<0.01
20	13	CSH	0.8122	<0.01	0.8072	<0.01
21	13	CSH	0.7494	<0.01	0.784	<0.01
22	12	OSH	0.7184	<0.01	0.7317	<0.01
23	29	MF	0.9003	<0.01	0.9274	<0.01
24	26	GRA	0.8585	<0.01	0.7947	<0.01
25	18	ENF	0.1245	>0.05	0.1838	>0.05
26	33	DBF	0.8161	<0.01	0.858	<0.01
27	32	OSH	0.3317	>0.05	0.1936	>0.05
28	33	SAV	0.4454	<0.05	0.4823	<0.05
29	8	GRA_{C4}	0.7285	<0.01	0.7162	<0.01
30	11	OSH	0.7718	<0.01	0.801	<0.01
Mean			0.4947		0.4787	

with g_c (Eq. (8)). This framework is a semi-mechanistic model for estimating g_c by combining theories on the photosynthetic pathway and optimal stomatal behavior. The results indicate that the relationship between SIF and $g_c \times VPD^{0.5}$ has improved performance over that between SIF and GPP (Fig. 4), accounting for the enhancement of VPD on the correlation of SIF-g_c. With an increase in VPD, the stomatal closure reduces the diffusion of CO_2 into the mesophyll, causing imbalances between carboxylation and the harvest of light, then reduces GPP and SIF (Paul-Limoges et al., 2018). Other mechanism models suggest that VPD may also optimize T retrieval through SIF (Feng et al., 2021), since VPD is a key parameter in the PM model and contributes to the explanation of large variability in the SIF-T relationship at the ecosystem scale (Jonard et al., 2020).

Considering that the SIF-$g_c \times VPD^{0.5}$ connection varies with PFTs (Shan et al., 2021), we calculated the model parameters *a* and *b* of the equation for each PFTs (Fig. 5 and Table 2). We find that the model slope of GRA_{C4} is much greater than that of GRA, which might be attributed to different photosynthetic strategies of C3 and C4 plants (Table 2). This may be because the GPP of C4 plants is more sensitive to SIF than that of C3 plants (Li et al., 2018; Liu et al., 2017), and C3 plants are more likely

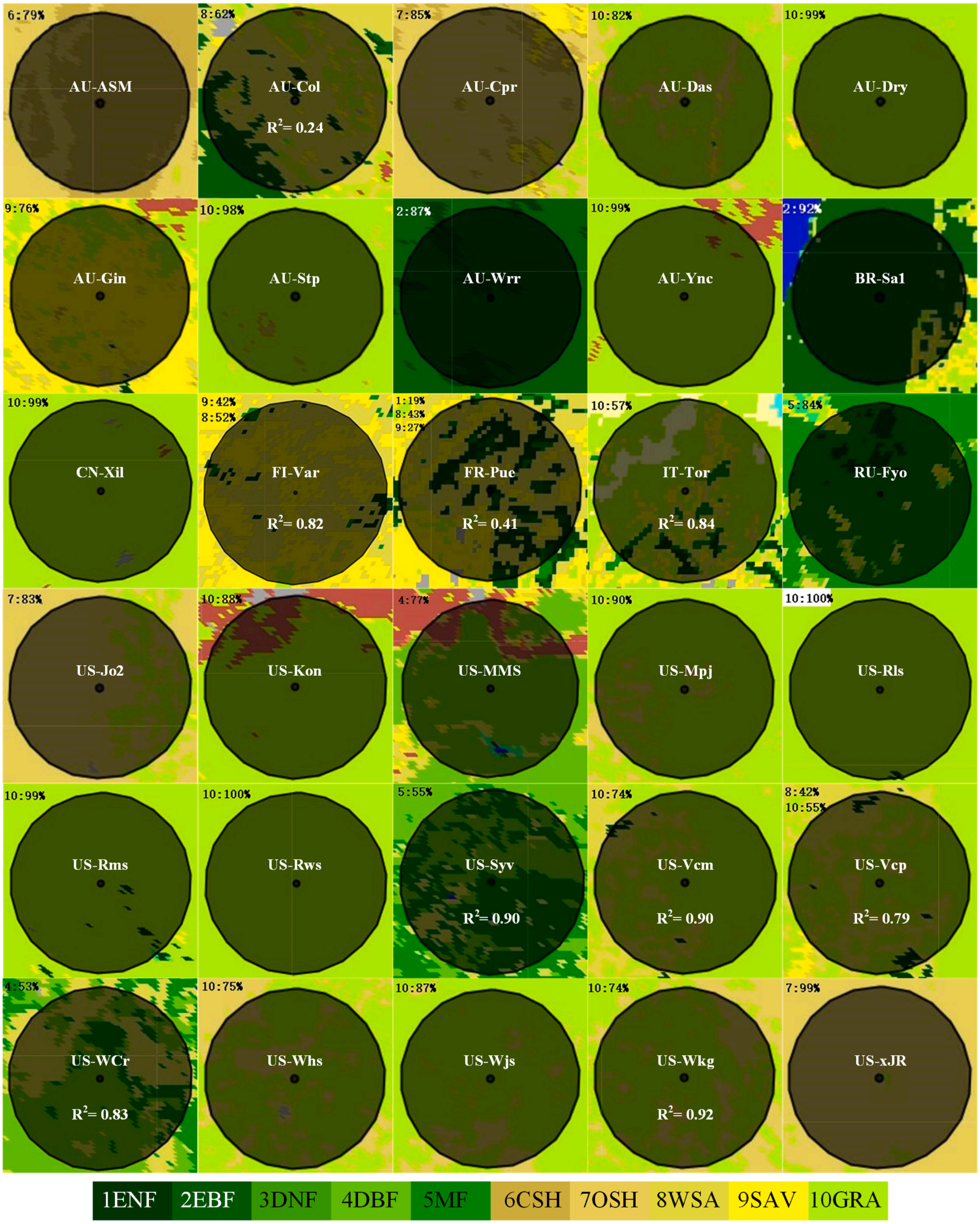

Fig. A1. Vegetation types of the 10-km buffer zone around each site. The first line in the upper left corner of each small plot represents the vegetation type of the site and its proportion within the 10-km buffer zone, and the other lines represent the proportion of other main vegetation types. When the vegetation type proportion of the site within the 10-km buffer is<75%, the correlation coefficient between LAI of the 1-km buffer and the 10-km buffer of the site are marked with white words below each site.

to exhibit a positive ET response than C4 plants (Massmann et al., 2019). Different PFTs within C3 plants differ in SIF, LAI and response to stress, and water stress stability in forests is much larger than in grasslands (Isbell et al., 2015; Zhang et al., 2019c). As a result, a calibration of the g_c-SIF model is also required for independent PFTs of C3 plants. Our results show that the SIF-$g_c \times VPD^{0.5}$ correlations are relatively weak in GRA and OSH because GPP, SIF and VPD in these PFTs with low vegetation coverage, are generally more vulnerable to environmental factors. The lower model slopes in these PFTs are probably due to a lower m value in the BBL model (Table 1). The *m* value varied among PFTs, especially for forests, due to the possibility that the big-leaf model applied in forests with a high LAI generally underestimates GPP

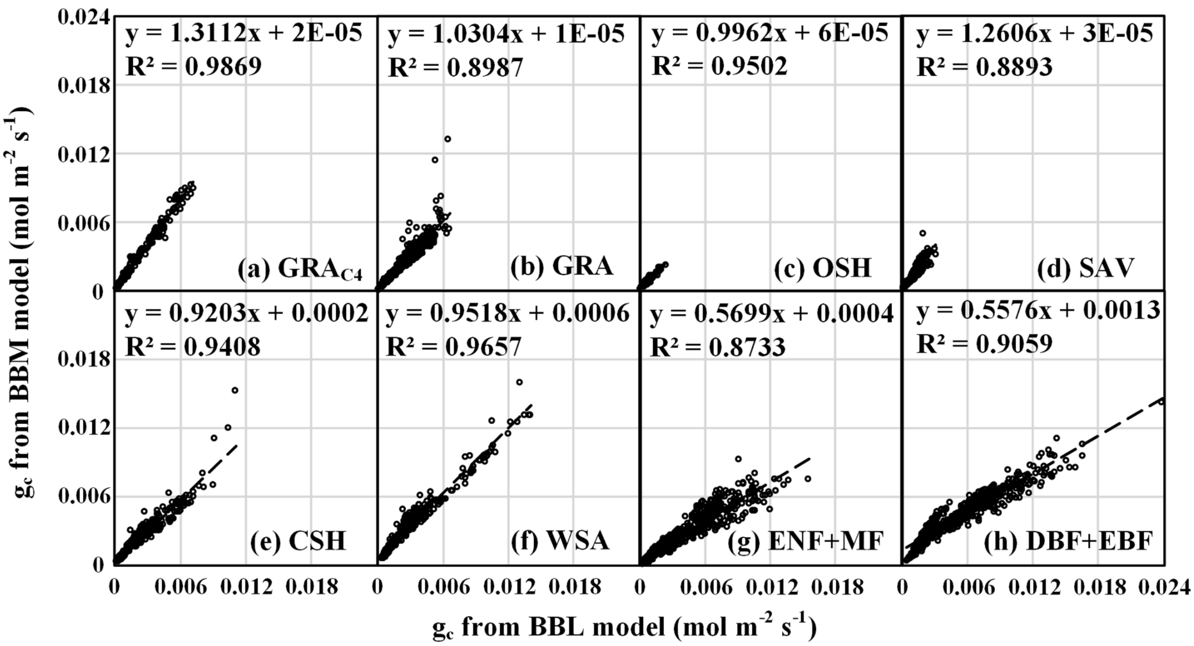

Fig. A2. The relationship of daily mean g_c between from the BBL model and from the BBM model. The fitted g0 and g1 values on the BBM model for different PFTs are from Lin et al. (2015), in which g0 is 0 for every PFTs, and g1 are 2.35 in ENF, 4.12 in EBF, 2.35 in DNF, 4.45 in DBF, 4.7 in Shrub, 5.25 in GRA, 1.62 in GRA$_{C4}$. The fitted g1 values in Sav and WSA are 4.8 and 6.7.

(Sprintsin et al., 2012).

The precipitation interception process has an important effect on the accuracy of T partitioning from ET. The inaccurate description of the interception process is one of the major reasons for the general underestimate of T/ET by climate models (Lian et al., 2018). In addition, the large difference in T/ET values from two isotope methods reported are mainly due to the disparate interception evaporation fluxes they used (Good et al., 2015; Jasechko et al., 2013). As for PM-MOD model, previous studies indicate its interception evaporation is much greater than that from other global ET products (i.e., GLEAM and PT-JPL) (Miralles et al., 2016). This is because the r_s of the wet canopy is underestimated in the PM-MOD model (Yue et al., 2021; Zhang et al., 2019a). In this study, our treatment of *I* is partially consistent with the PM-MOD model by distinguishing wet and dry surfaces, but we simply remove the energy of interception evaporation, independent of the resistance, implying that our treatment of the interception process has less effect on the partitioning of T from ET.

Moreover, our results show that the correlation between SIF and $g_c \times VPD^{0.5}$ is more robust at a coarser temporal scale (Figs. 4 & 5), which is similar to previous works on the more linear relationship between GPP and SIF from short to longer time scales (Frankenberg et al., 2011; Yang et al., 2017). This temporal aggregation effect is also observed in the SIF-T relationship in the temperate forest ecosystem (Lu et al., 2018), which suggests that both SIF and $g_c \times VPD^{0.5}$ are sensitive to other environmental factors in different ways.

4.2. Comparison with other independent ET partitioning products

We compare T/ET across different PFTs at the site scale and find a trend toward a higher T/ET for PFTs with higher vegetation coverage (Figs. 6 & 7). This trend coincides with the nonlinear relationship between T/ET and LAI found by Wang et al. (2014) and Wei et al. (2017). However, this trend has been challenged in high LAI ecosystems, with a close T/ET value (0.78) for ENF and EBF (Figs. 6 & 7). The underlying mechanism is that more precipitation interception of broad-leaved forests results in an increased *I* than that of coniferous forests during the growing season (van Dijk et al., 2015). For grasslands, significant differences in T/ET are observed between our study and Wei et al. (2017), primarily derived from photosynthetic pathways. The T/ET of GRA$_{C3}$ is much lower than that of GRA$_{C4}$ (Fig. 6). Compared with GRA$_{C3}$, GRA$_{C4}$ has a very low Γ and can sustain photosynthesis with very low g_c under conditions of high atmospheric water demand and limited water availability (Brooks and Farquhar, 1985). This may cause C4 plants to maintain low g_c and T, and to continue emitting SIF under water stress. Our study and Wei et al. (2017) indicate that the T/ET for SAV, WSA and shrublands (OSH and CSH) is about 0.6 with a large standard deviation (Fig. 7). Statistically, the large standard deviation is due to the small sample size and the occurrence of outliers (Fig. 7). The large standard deviation causes the PFT-mean pattern of SAV, WSA and shrublands to be opposite to the PFT-median pattern, and the PFT-median pattern is in line with Wei et al. (2017). If using more sites in the future comparison, it is expected the discrepancy of PFT-mean pattern in T/ET ratio for SAV, WSA and shrublands between our and Wei's results may not exist. Ecologically, the large standard deviation may be because in SAV, WSA and shrublands, surface landscape heterogeneity affects the fraction of absorbed PAR by leaves and further eco-hydrological processes, particularly T (Kobayashi et al., 2012). Besides, the large standard deviation may also be due to the distinct patterns of carbon–water coupling between herbaceous and woody plants in SAV, WSA and shrublands (Wei et al., 2017). Moreover, SAV, WSA and shrublands are usually vegetated sparsely, which may result in a situation where E predominates over T.

We collected the results of global mean T/ET derived from 36 different methods (Table 3). The estimated global mean T/ET is>50% for most methods. Our global mean T/ET value of 0.57 closes to the ensemble mean of global T/ET (0.549) from these different methods. Climate models generally underestimate the global mean T/ET due to the inaccuracies in their representation of canopy light use and root water uptake processes (Lian et al., 2018). Hydrological processes-based climate models, such as ParFlow-CLM (Maxwell and Condon, 2016) and T&C (Fatichi and Pappas, 2017) generally calculate a greater T/ET than the other models. Global mean T/ET values derived from isotopes, LAI-based models, remote sensing models and WUE-based models are all around 0.6, which are slightly higher than our results. The lower value in our study may be because we compare T/ET on different timescales.

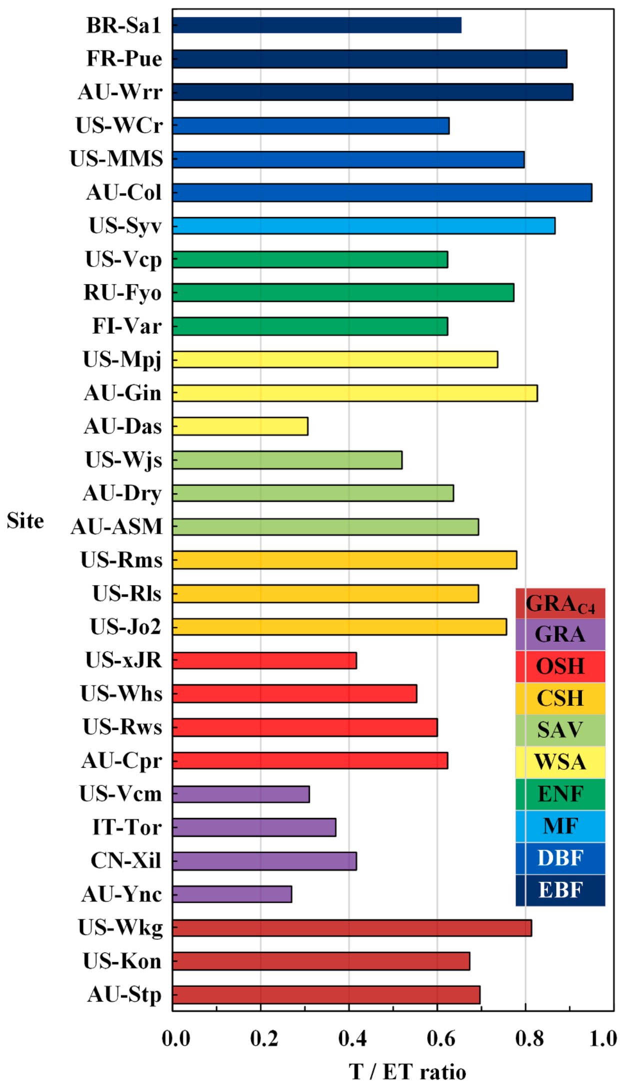

Fig. A3. The T/ET for each site calculated using the BBL model.

Growing season with sufficient precipitation generally leads to an increased I and hence a drop in T/ET, particularly for forests. The lower T/ET in our study may also be a consequence of the neglect of the impact of C4 plants and crops when upscaling T/ET to the global terrestrial ecosystem. They generally have a greater T/ET value than C3 plants. The greater T/ET achieved using isotope method may be due to the significant uncertainties of isotopic ratios under weak turbulence conditions (Wei et al., 2015) or the overestimation of T in cases of hydrologic decoupling (Brooks et al., 2010). The greater T/ET value derived using LAI-based model, especially the method of Wang et al. (2014), is most likely attributed to the inadequacy of the statistical method used to calculate global average, which is simply an arithmetic average of all observations. The global per-pixel calculation method (Wei et al., 2017) and the weighted average method (this study) (Schlesinger and Jasechko, 2014) are more acceptable. There are two possible explanations for the greater T/ET value calculated by Li et al. (2019) in the WUE-based model: the statistical method used and the omission of I.

When compared to remote sensing models, our method produces comparable global mean T/ET values as PT-JPT and PML-V2, whereas GLEAM, PML and Gerrits's model generate larger global mean T/ET values and PM-MOD has a lower global mean T/ET value. GLEAM and Gerrits's model have approximate estimation of T and ET (Mianabadi et al., 2019). A comparative study finds that PT-JPT is the closest to the actual T/ET value, while GLEAM (PM-MOD) overestimates (underestimates) T/ET based on field observations (Talsma et al., 2018). Another reason for underestimating T/ET by PM-MOD is that it significantly overestimates I as shown in section 4.1. GLEAM substantially underestimates soil evaporation but slightly overestimates T, resulting in a high accuracy of ET estimates (Talsma et al., 2018). This perspective coincides with our findings that the T estimates in GLEAM are systematically greater than our global simulations (Figs. 8 & 10). The most possible reason why PML has a larger global mean T/ET value than our result is that PML overestimate T since the g_c of PML is calculated through empirical equations based on LAI and PAR without considering water and heat stresses (Leuning et al., 2008). Thus, based on PML, the PML-V2 optimizes the original g_c module into the Ball-Berry model with carbon–water coupling characteristics (Gan et al., 2018). The PML-V2 has been proved to perform better in estimating GPP and ET (Zhang et al., 2019b). The estimation of T illustrates that our result is consistent with PML-V2 at the site scale (Fig. 8). Nevertheless, when compared to PML-V2, our global patterns of T indicate that it is larger in the tropics and lower in the drylands (Fig. 10). The explanation may include the following aspects: 1) The relationship between SIF and the modeled GPP varies in these two regions; 2) We estimate T by treating C4 plants as C3 plants; 3) The available energy for T in our model is different from PML-V2.

4.3. Implications and limitations

Our study may have important implications for assessing regional and global water flux under climate change. This new framework reveals that satellite SIF may be utilized to precisely estimate T/ET and monitor the spatio-temporal variations in terrestrial T at the regional and global scale combined with meteorological data (Figs. 7 & 9). The T/ET value calculated using SIF can help to resolve whether T/ET is constrained by vegetation characteristics and environmental factors (Fatichi and Pappas, 2017; Niu et al., 2019; Paschalis et al., 2018; Wei et al., 2017). In addition, previous empirical techniques employing vegetation indexes or LAI can produce T, but hardly capture the temporal variations of T since they are limited to environmental conditions and ecosystems (Zhang et al., 2016a). Our SIF-based approach is useful to resolve this shortcoming because SIF is more sensitive than other remotely sensed vegetation parameters to plant photosynthetic and water/heat stresses (Song et al., 2018; Yoshida et al., 2015). A remotely sensed ET model with better performance can be developed in association with appropriate remote sensing models for I and E. This could be used to improve the simulation accuracy of the global water and energy cycle.

However, there are still some limitations in this study. First, our method may be inapplicable in the condition of carbon–water decoupling. For example, forests may decouple photosynthesis and T in response to heat extremes and sufficient water availability (De Kauwe et al., 2019). The trade-off between leaf water potential regulation and stomatal behavior may influence the effect of VPD on the SIF-g_c relationship (Martinez-Vilalta and Garcia-Forner, 2017). Second, the classification of PFTs is inadequate and needs further refined. The remote sensing methods for T retrieval, such as PM-MOD, generally divide the global ecosystem into 11 or more PFTs (Mu et al., 2011). Our model examines 10 PFTs and did not distinguish crops or wetlands. Moreover, we do not consider the proportion of C4 grasslands in our global T simulation due to lack of accurate global map of C4 plants, even though we have developed models for C4 grasslands. Third, the validation of our model may be limited by the source of validated data. While we validated our results from satellite SIF data using EC flux tower and other remote sensing products, the flux tower T/ET is achieved by simulation, not by independent field measurements such as the isotope method.

5. Conclusion

Our results show that SIF has a stronger relationship with $g_c \times VPD^{0.5}$

Table B1
All abbreviations and their meanings in this study.

Abbreviation	Full name	Abbreviation	Full name	Abbreviation	Full name
a	slope for the linear relationships between $g_c \times VPD^{0.5}$ and SIF for each PFT	**GLEAM**	Global Land Evaporation Amsterdam Model	**$R_l\downarrow$**	downward thermal radiation
A_n	net assimilation rate or gross photosynthesis	**GPP**	vegetation productivity	**$R_l\uparrow$**	upward thermal radiation
b	intercept for the linear relationships between $g_c \times VPD^{0.5}$ and SIF for each PFT	**GRA**	C3 grasslands	**RMSE**	root mean square error
BBL	Ball-Berry-Leuning	**GRA_{C4}**	C4 grasslands	**R_n**	net radiation
c_p	specific heat of the air	**G_s**	surface conductance	**R_{nl}**	surface net thermal radiation
CO_2	carbon dioxide	**h_c**	canopy height	**R_{ns}**	surface net solar radiation
C_s	$[CO_2]$ at the leaf surface	**h_m**	measurement height	**$R_s\downarrow$**	downward solar radiation
$[CO_2]$	CO2 concentration	**I**	interception evaporation	**$R_s\uparrow$**	upward solar radiation
CSH	closed shrublands	**LAI**	leaf area index	**SAV**	savannas
DBF	deciduous broadleaf forests	**LE**	latent heat flux	**SIF**	solar-induced chlorophyll fluorescence
D_0	an empirically fitted parameter representing the sensitivity of stomata to changes in D_s	**m**	slope in BBL model calculated from empirical data	**T**	transpiration
D_s	humidity deficit at the leaf surface	**MAE**	mean absolute error	**T_{air}**	2 m temperature
e_{sat}	saturated vapor pressure	**MF**	mixed forests	**T_{dew}**	2 m dewpoint temperature
$e_{sat,dew}$	e_{sat} at dew point temperature	**MODIS**	moderate resolution imaging spectroradiometer	**T_{SITE}**	T calculated using g_{cSITE}
E	evaporation	**MSE**	mean square error	**T_{SIF}**	T calculated using g_{cSIF}
EBF	evergreen broadleaf forests	**OSH**	open shrublands	**T/ET**	ratio of T to ET
ECMWF	European Centre for Medium-Range Weather Forecasts	**P**	surface pressure	**T_{SITE}/ET**	ratio of T_{SITE} to ET
ENF	evergreen needle forests	**PAR**	photosynthetically active radiation	**T_{SIF}/ET**	ratio of T_{SIF} to ET
ERA5-Land	the 5th ECMWF reanalysis for land	**PFT**	plant functional type	**TROPOMI**	TROPOspheric Monitoring Instrument
ET	evapotranspiration	**PM**	Penman-Monteith model	**u**	wind speed
fPAR	fraction of PAR absorbed by vegetation	**PML**	Penman-Monteith-Leuning model	**u***	friction velocity
f_{wet}	wet surface fraction	**PML-V2**	Penman-Monteith-Leuning-Version 2 model	**V_m**	coefficient when converting g_s from mol m^{-2} s^{-1} to m s^{-1}
g_0	minimum conductance in BBL model calculated from empirical data	**PM_{opt}**	optimized Penman-Monteith model	**VPD**	vapor pressure deficit
g_c	canopy conductance	**PM-MOD**	MODIS evapotranspiration model	**WSA**	woody savannas
g_{cSITE}	g_c calculated using BBL model	**PT-JPL**	Priestley-Taylor Jet Propulsion Laboratory model	**WUE**	water-use efficiency
g_{cSIF}	g_c calculated using g_c-SIF model	**r_a**	aerodynamic resistance	**Δ**	slope of the saturation vapour pressure temperature relationship
g_c-SIF model	PFT-specific SIF-driven semi-mechanism gc model	**r_s**	surface resistance	**Γ**	CO_2 compensation point
g_s	stomatal conductance	**R**	Pearson's correlation coefficient	**γ**	psychrometric constant
G	ground heat flux	**R^2**	goodness of fit	**λ**	latent heat of vaporization
GEE	google earth engine	**RH**	air relative humidity	**ρ_a**	mean air density at constant pressure

than GPP, and the SIF-$g_c \times VPD^{0.5}$ linear regression at the 16-day scale are tighter and sharper than at the daily scale. Based on the regression, we developed the SIF-driven semi-mechanism g_c model on various PFTs and use the PM_{opt} model to calculate T and T/ET. Correlations between T_{SIF}/ET and T/ET values from other independent techniques are excellent at both site and global scale. After the implementation of our g_c-SIF model, we estimate the global mean T/ET of the terrestrial ecosystem for growing season in 2018 (0.57 ± 0.14) that is close to the mean T/ET value (0.55) of the current models from other 36 methods. Ultimately, we simulate global T for the 2018 growing season at the resolution of 0.1° × 0.1°and compare it to two commonly used remote sensing retrieval products. Our model provides a valuable complement to remote sensing-based T and ET retrieval, and has critical implications for assessing eco-hydrological processes under climate change. More consideration about condition of carbon–water decoupling, different PFTs, and source of validated data will be useful in future studies.

CRediT authorship contribution statement

Yaojie Liu: Methodology, Software, Validation, Formal analysis, Investigation, Data curation, Writing – original draft, Visualization. **Yongguang Zhang:** Conceptualization, Resources, Writing – review & editing, Supervision, Project administration, Funding acquisition. **Nan Shan:** Methodology, Writing – review & editing. **Zhaoying Zhang:** Resources, Data curation, Writing – review & editing, Funding acquisition. **Zhongwang Wei:** Validation, Resources, Writing – review & editing.

Declaration of Competing Interest

The authors declare that they have no known competing financial interests or personal relationships that could have appeared to influence the work reported in this paper.

Acknowledgments

All authors approved this paper submission to the *Journal of Hydrology* and declare no conflict of interest. This research is financially supported by the National Natural Science Foundation of China (NSFC) (42125105, 42071388), and the Youth Program of NSFC (42101320). The authors acknowledge the European Centre for Medium-Range Weather Forecasts for the ERA5 data, and the FLUXNET community, including the following: AmeriFlux, the European Eddy Fluxes Database Cluster, ChinaFlux, and OzFlux-TERN, for the eddy covariance data. Martens Brecht and Miralles Diego G. are acknowledged for providing GLEAM data via https://www.gleam.eu/. The research team of Zhang

Yongqiang is acknowledged for providing PML-V2 data via GEE. We also acknowledge Philipp Köhler and Christian Frankenberg for providing TROPOMI SIF. TROPOMI SIF is available at ftp://fluo.gps.caltech.edu/data/tropomi/. The MODIS products used here are available via GEE.

Appendix A. . The information and supplementary results of the FLUXNET sites used in this study

Appendix B. The abbreviations used in this study.

References

Alton, P., Fisher, R., Los, S., Williams, M., 2009. Simulations of global evapotranspiration using semiempirical and mechanistic schemes of plant hydrology. Global Biogeochem. Cy. 23 (4) https://doi.org/10.1029/2009GB003540.

Brooks, J.R., Barnard, H.R., Coulombe, R., McDonnell, J.J., 2010. Ecohydrologic separation of water between trees and streams in a Mediterranean climate. Nat. Geosci. 3 (2), 100–104. https://doi.org/10.1038/ngeo722.

Brooks, A., Farquhar, G.D., 1985. Effect of temperature on the CO_2/O_2 specificity of ribulose-1,5-bisphosphate carboxylase oxygenase and the rate of respiration in the light-estimates from gas-exchange measurements on spinach. Planta. 165 (3), 397–406. https://doi.org/10.1007/bf00392238.

Cao, L., Bala, G., Caldeira, K., Nemani, R., Ban-Weiss, G., 2010. Importance of carbon dioxide physiological forcing to future climate change. Proc. Natl. Acad. Sci. U. S. A. 107 (21), 9513–9518. https://doi.org/10.1073/pnas.0913000107.

Chen, J.M., Mo, G., Pisek, J., Liu, J., Deng, F., Ishizawa, M., Chan, D., 2012. Effects of foliage clumping on the estimation of global terrestrial gross primary productivity. Global Biogeochem. Cy. 26 (1) https://doi.org/10.1029/2010GB003996.

Choudhury, B.J., DiGirolamo, N.E., 1998. A biophysical process-based estimate of global land surface evaporation using satellite and ancillary data I. Model description and comparison with observations. J. Hydrol. 205 (3–4), 164–185. https://doi.org/10.1016/S0022-1694(97)00147-9.

Coenders-Gerrits, A.M.J., van der Ent, R.J., Bogaard, T.A., Wang-Erlandsson, L., Hrachowitz, M., Savenije, H.H.G., 2014. Uncertainties in transpiration estimates. Nature 506 (7487), E1–E2. https://doi.org/10.1038/nature12925.

Compo, G.P., Whitaker, J.S., Sardeshmukh, P.D., Matsui, N., Allan, R.J., Yin, X., Gleason, B.E., Vose, R.S., Rutledge, G., Bessemoulin, P., Brönnimann, S., Brunet, M., Crouthamel, R.I., Grant, A.N., Groisman, P.Y., Jones, P.D., Kruk, M.C., Kruger, A.C., Marshall, G.J., Maugeri, M., Mok, H.Y., Nordli, Ø., Ross, T.F., Trigo, R.M., Wang, X. L., Woodruff, S.D., Worley, S.J., 2011. The twentieth century reanalysis project. Q. J. Roy. Meteor. Soc. 137 (654), 1–28. https://doi.org/10.1002/qj.776.

Damm, A., Roethlin, S., Fritsche, L., IEEE, 2018. Towards advanced retrievals of plant transpiration using sun-induced chlorophyll fluorescence: first considerations. In: IGARSS 2018–2018 IEEE International Geoscience and Remote Sensing Symposium, pp. 5983–5986. https://doi.org/10.1109/IGARSS.2018.8518974.

De Kauwe, M.G., Kala, J., Lin, Y.S., Pitman, A.J., Medlyn, B.E., Duursma, R.A., Abramowitz, G., et al., 2015. A test of an optimal stomatal conductance scheme within the CABLE land surface model. Geosci. Model Dev. 8 (2), 431–452. https://doi.org/10.5194/gmd-8-431-2015.

De Kauwe, M.G., Medlyn, B.E., Pitman, A.J., Drake, J.E., Ukkola, A., Griebel, A., Pendall, E., Prober, S., Roderick, M., 2019. Examining the evidence for decoupling between photosynthesis and transpiration during heat extremes. Biogeosciences 16 (4), 903–916. https://doi.org/10.5194/bg-16-903-2019.

Dirmeyer, P.A., Gao, X., Zhao, M., Guo, Z.C., Oki, T., Hanasaki, N., 2006. GSWP-2: Multimodel analysis and implications for our perception of the land surface. B. Am. Meteorol. Soc. 87 (10), 1381–1398. https://doi.org/10.1175/BAMS-87-10-1381.

ECMWF, 2017. ERA5 Reanalysis [Date set]. In: Forecasts (Ed.), Research Data Archive at the National Center for Atmospheric Research, Computational and. Information Systems Laboratory, Boulder, CO. https://doi.org/10.5065/D6X34W69.

Fatichi, S., Pappas, C., 2017. Constrained variability of modeled T:ET ratio across biomes. Geophys. Res. Lett. 44 (13), 6795–6803. https://doi.org/10.1002/2017gl074041.

Feng, H., Xu, T., Liu, L., Zhou, S., Zhao, J., Liu, S., Xu, Z., Mao, K., He, X., Zhu, Z., Chai, L., 2021. Modeling Transpiration with Sun-Induced Chlorophyll Fluorescence Observations via Carbon-Water Coupling Methods. Remote Sens. 13 (4), 804. https://doi.org/10.3390/rs13040804.

Fisher, J.B., Tu, K.P., Baldocchi, D.D., 2008. Global estimates of the land-atmosphere water flux based on monthly AVHRR and ISLSCP-II data, validated at 16 FLUXNET sites. Remote Sens. Environ. 112 (3), 901–919. https://doi.org/10.1016/j.rse.2007.06.025.

Frankenberg, C., Butz, A., Toon, G.C., 2011. Disentangling chlorophyll fluorescence from atmospheric scattering effects in O_2 A-band spectra of reflected sun-light. Geophys. Res. Lett. 38 (3) https://doi.org/10.1029/2010GL045896.

Friedl, M.A., Sulla-Menashe, D., Tan, B., Schneider, A., Ramankutty, N., Sibley, A., Huang, X., 2010. MODIS Collection 5 global land cover: Algorithm refinements and characterization of new datasets. Remote Sens. Environ. 114 (1), 168–182. https://doi.org/10.1016/j.rse.2009.08.016.

Gan, R., Zhang, Y.Q., Shi, H., Yang, Y.T., Eamus, D., Cheng, L., Chiew, F.H.S., Yu, Q., 2018. Use of satellite leaf area index estimating evapotranspiration and gross assimilation for Australian ecosystems. Ecohydrology. 11 (5), 15. https://doi.org/10.1002/eco.1974.

Gerten, D., Hoff, H., Bondeau, A., Lucht, W., Smith, P., Zaehle, S., 2005. Contemporary "green" water flows: Simulations with a dynamic global vegetation and water balance model. Phys. Chem. Earth. Pt. A/B/C. 30 (6–7), 334–338. https://doi.org/10.1016/j.pce.2005.06.002.

Good, S.P., Noone, D., Bowen, G., 2015. Hydrologic connectivity constrains partitioning of global terrestrial water fluxes. Science. 349 (6244), 175–177. https://doi.org/10.1126/science.aaa5931.

Guanter, L., Zhang, Y., Jung, M., Joiner, J., Voigt, M., Berry, J.A., Frankenberg, C., Huete, A.R., Zarco-Tejada, P., Lee, J.-E., Moran, M.S., Ponce-Campos, G., Beer, C., Camps-Valls, G., Buchmann, N., Gianelle, D., Klumpp, K., Cescatti, A., Baker, J.M., Griffis, T.J., 2014. Global and time-resolved monitoring of crop photosynthesis with chlorophyll fluorescence. Proc. Natl. Acad. Sci. U. S. A. 111 (14) https://doi.org/10.1073/pnas.1320008111.

Huang, S.Y., Deng, Y., Wang, J.F., 2017. Revisiting the global surface energy budgets with maximum-entropy-production model of surface heat fluxes. Clim. Dynam. 49 (5), 1531–1545. https://doi.org/10.1007/s00382-016-3395-x.

Isbell, F., Craven, D., Connolly, J., Loreau, M., Schmid, B., Beierkuhnlein, C., Bezemer, T. M., Bonin, C., Bruelheide, H., de Luca, E., Ebeling, A., Griffin, J.N., Guo, Q., Hautier, Y., Hector, A., Jentsch, A., Kreyling, J., Lanta, V., Manning, P., Meyer, S.T., Mori, A.S., Naeem, S., Niklaus, P.A., Polley, H.W., Reich, P.B., Roscher, C., Seabloom, E.W., Smith, M.D., Thakur, M.P., Tilman, D., Tracy, B.F., van der Putten, W.H., van Ruijven, J., Weigelt, A., Weisser, W.W., Wilsey, B., Eisenhauer, N., 2015. Biodiversity increases the resistance of ecosystem productivity to climate extremes. Nature. 526 (7574), 574–577. https://doi.org/10.1038/nature15374.

Ito, A., Inatomi, M., 2012. Water-use efficiency of the terrestrial biosphere: a model analysis focusing on interactions between the global carbon and water cycles. Journal of Hydrometeorology 13 (2), 681–694. https://doi.org/10.1175/JHM-D-10-05034.1.

Jasechko, S., Sharp, Z.D., Gibson, J.J., Birks, S.J., Yi, Y., Fawcett, P.J., 2013. Terrestrial water fluxes dominated by transpiration. Nature. 496 (7445), 347-+. https://doi.org/10.1038/nature11983.

Joiner, J., Yoshida, Y., Vasilkov, A.P., Yoshida, Y., Corp, L.A., Middleton, E.M., 2011. First observations of global and seasonal terrestrial chlorophyll fluorescence from space. Biogeosciences 8 (3), 637–651. https://doi.org/10.5194/bg-8-637-2011.

Jonard, F., De Cannière, S., Brüggemann, N., Gentine, P., Short Gianotti, D.J., Lobet, G., Miralles, D.G., Montzka, C., Pagán, B.R., Rascher, U., Vereecken, H., 2020. Value of sun-induced chlorophyll fluorescence for quantifying hydrological states and fluxes: Current status and challenges. Agr. For. Meteorol. 291, 108088. https://doi.org/10.1016/j.agrformet.2020.108088.

Jung, M., Reichstein, M., Ciais, P., Seneviratne, S.I., Sheffield, J., Goulden, M.L., Bonan, G., Cescatti, A., Chen, J., de Jeu, R., Dolman, A.J., Eugster, W., Gerten, D., Gianelle, D., Gobron, N., Heinke, J., Kimball, J., Law, B.E., Montagnani, L., Mu, Q., Mueller, B., Oleson, K., Papale, D., Richardson, A.D., Roupsard, O., Running, S., Tomelleri, E., Viovy, N., Weber, U., Williams, C., Wood, E., Zaehle, S., Zhang, K.e., 2010. Recent decline in the global land evapotranspiration trend due to limited moisture supply. Nature. 467 (7318), 951–954. https://doi.org/10.1038/nature09396.

Kobayashi, H., Baldocchi, D.D., Ryu, Y., Chen, Q., Ma, S.Y., Osuna, J.L., Ustin, S.L., 2012. Modeling energy and carbon fluxes in a heterogeneous oak woodland: A three-dimensional approach. Agr. For. Meteorol. 152, 83–100. https://doi.org/10.1016/j.agrformet.2011.09.008.

Kool, D., Agam, N., Lazarovitch, N., Heitman, J.L., Sauer, T.J., Ben-Gal, A., 2014. A review of approaches for evapotranspiration partitioning. Agr. For. Meteorol. 184, 56–70. https://doi.org/10.1016/j.agrformet.2013.09.003.

Köhler, P., Frankenberg, C., Magney, T.S., Guanter, L., Joiner, J., Landgraf, J., 2018. Global retrievals of solar-induced chlorophyll fluorescence with TROPOMI: First results and intersensor comparison to OCO-2. Geophys. Res. Lett. 45 (19), 10456–10463. https://doi.org/10.1029/2018GL079031.

Lasslop, G., Reichstein, M., Detto, M., Richardson, A.D., Baldocchi, D.D., 2010. Comment on Vickers et al.: Self-correlation between assimilation and respiration resulting from flux partitioning of eddy-covariance CO_2 fluxes. Agr. For. Meteorol. 150 (2), 312–314. https://doi.org/10.1016/j.agrformet.2009.11.003.

Lawrence, D.M., Oleson, K.W., Flanner, M.G., Thornton, P.E., Swenson, S.C., Lawrence, P.J., Zeng, X., Yang, Z.-L., Levis, S., Sakaguchi, K., Bonan, G.B., Slater, A. G., 2011. Parameterization improvements and functional and structural advances in version 4 of the Community Land Model. J. Adv. Model Earth Sy. 3 (1) https://doi.org/10.1029/2011MS00045.

Lawrence, D.M., Thornton, P.E., Oleson, K.W., Bonan, G.B., 2007. The partitioning of evapotranspiration into transpiration, soil evaporation, and canopy evaporation in a GCM: Impacts on land–atmosphere interaction. J. Hydrometeorol. 8 (4), 862–880. https://doi.org/10.1175/JHM596.1.

Leuning, R., 1995. A critical appraisal of a combined stomatal-photosynthesis model for C3 plants. Plant Cell Environ. 18 (4), 339–355. https://doi.org/10.1111/j.1365-3040.1995.tb00370.x.

Leuning, R., Zhang, Y.Q., Rajaud, A., Cleugh, H., Tu, K., 2008. A simple surface conductance model to estimate regional evaporation using MODIS leaf area index and the Penman-Monteith equation. Water Resour. Res. 44 (10), 17. https://doi.org/10.1029/2007wr006562.

Li, X., Gentine, P., Lin, C.J., Zhou, S., Sun, Z., Zheng, Y., Liu, J., Zhang, C.M., 2019. A simple and objective method to partition evapotranspiration into transpiration and

evaporation at eddy-covariance sites. Agr. For. Meteorol. 265, 171–182. https://doi.org/10.1016/j.agrformet.2018.11.017.
Li, X., Xiao, J., He, B., Altaf Arain, M., Beringer, J., Desai, A.R., Emmel, C., Hollinger, D. Y., Krasnova, A., Mammarella, I., Noe, S.M., Ortiz, P.S., Rey-Sanchez, A.C., Rocha, A. V., Varlagin, A., 2018. Solar-induced chlorophyll fluorescence is strongly correlated with terrestrial photosynthesis for a wide variety of biomes: First global analysis based on OCO-2 and flux tower observations. Global Change Biol. 24 (9), 3990–4008. https://doi.org/10.1111/gcb.14297.
Lian, X.u., Piao, S., Huntingford, C., Li, Y., Zeng, Z., Wang, X., Ciais, P., McVicar, T.R., Peng, S., Ottlé, C., Yang, H., Yang, Y., Zhang, Y., Wang, T., 2018. Partitioning global land evapotranspiration using CMIP5 models constrained by observations. Nat. Clim. Change 8 (7), 640–646. https://doi.org/10.1038/s41558-018-0207-9.
Lin, Y.-S., Medlyn, B.E., Duursma, R.A., Prentice, I.C., Wang, H., Baig, S., Eamus, D., de Dios, V., Mitchell, P., Ellsworth, D.S., de Beeck, M.O., Wallin, G., Uddling, J., Tarvainen, L., Linderson, M.-L., Cernusak, L.A., Nippert, J.B., Ocheltree, T.W., Tissue, D.T., Martin-StPaul, N.K., Rogers, A., Warren, J.M., De Angelis, P., Hikosaka, K., Han, Q., Onoda, Y., Gimeno, T.E., Barton, C.V.M., Bennie, J., Bonal, D., Bosc, A., Löw, M., Macinins-Ng, C., Rey, A., Rowland, L., Setterfield, S.A., Tausz-Posch, S., Zaragoza-Castells, J., Broadmeadow, M.S.J., Drake, J.E., Freeman, M., Ghannoum, O., Hutley, L., Kelly, J.W., Kikuzawa, K., Kolari, P., Koyama, K., Limousin, J.-M., Meir, P., Lola da Costa, A.C., Mikkelsen, T.N., Salinas, N., Sun, W., Wingate, L., 2015. Optimal stomatal behaviour around the world. Nat. Clim. Change. 5 (5), 459–464. https://doi.org/10.1038/nclimate2550.
Liu, L.Y., Guan, L.L., Liu, X.J., 2017. Directly estimating diurnal changes in GPP for C3 and C4 crops using far-red sun-induced chlorophyll fluorescence. Agr. For. Meteorol. 232, 1–9. https://doi.org/10.1016/j.agrformet.2016.06.014.
Lu, X.L., Liu, Z.Q., An, S.Q., Miralles, D.G., Maes, W.H., Liu, Y.L., Tang, J.W., 2018. Potential of solar-induced chlorophyll fluorescence to estimate transpiration in a temperate forest. Agr. For. Meteorol. 252, 75–87. https://doi.org/10.1016/j.agrformet.2018.01.017.
Maes, W.H., Pagán, B.R., Martens, B., Gentine, P., Guanter, L., Steppe, K., Verhoest, N.E. C., Dorigo, W., Li, X., Xiao, J., Miralles, D.G., 2020. Sun-induced fluorescence closely linked to ecosystem transpiration as evidenced by satellite data and radiative transfer models. Remote Sens. Environ. 249, 112030. https://doi.org/10.1016/j.rse.2020.112030.
Marshall, M., Thenkabail, P., Biggs, T., Post, K., 2016. Hyperspectral narrowband and multispectral broadband indices for remote sensing of crop evapotranspiration and its components (transpiration and soil evaporation). Agr. For. Meteorol. 218, 122–134. https://doi.org/10.1016/j.agrformet.2015.12.025.
Martens, B., Miralles, D.G., Lievens, H., van der Schalie, R., de Jeu, R.A.M., Fernández-Prieto, D., Beck, H.E., et al., 2017. GLEAM v3: Satellite-based land evaporation and root-zone soil moisture. Geosci. Model Dev. 10 (5), 1903–1925. https://doi.org/10.5194/gmd-10-1903-2017.
Martinez-Vilalta, J., Garcia-Forner, N., 2017. Water potential regulation, stomatal behaviour and hydraulic transport under drought: deconstructing the iso/anisohydric concept. Plant Cell Environ. 40 (6), 962–976. https://doi.org/10.1111/pce.12846.
Massmann, A., Gentine, P., Lin, C.J., 2019. When Does Vapor Pressure Deficit Drive or Reduce Evapotranspiration? J. Adv. Model. Earth Syst. 11 (10), 3305–3320. https://doi.org/10.1029/2019ms001790.
Maxwell, R.M., Condon, L.E., 2016. Connections between groundwater flow and transpiration partitioning. Science. 353 (6297), 377–380. https://doi.org/10.1126/science.aaf7891.
Medlyn, B.E., Duursma, R.A., Eamus, Derek, Ellsworth, D.S., Prentice, I.C., Barton, C.V. M., Crous, K.Y., De angelis, Paolo, Freeman, Michael, Wingate, Lisa, 2011. Reconciling the optimal and empirical approaches to modelling stomatal conductance. Global Change Biol. 17 (6), 2134–2144. https://doi.org/10.1111/j.1365-2486.2010.02375.x.
Mianabadi, A., Coenders-Gerrits, M., Shirazi, P., Ghahraman, B., Alizadeh, A., 2019. A global Budyko model to partition evaporation into interception and transpiration. Hydrol. Earth Syst. Sci. 23 (12), 4983–5000. https://doi.org/10.5194/hess-23-4983-2019.
Milly, P.C.D., Dunne, K.A., Vecchia, A.V., 2005. Global pattern of trends in streamflow and water availability in a changing climate. Nature. 438 (7066), 347–350. https://doi.org/10.1038/nature04312.
Miralles, D.G., De Jeu, R.A.M., Gash, J.H., Holmes, T.R.H., Dolman, A.J., 2011. Magnitude and variability of land evaporation and its components at the global scale. Hydrol. Earth Syst. Sci. 15 (3), 967–981. https://doi.org/10.5194/hess-15-967-2011.
Miralles, D.G., Jimenez, C., Jung, M., Michel, D., Ershadi, A., McCabe, M.F., et al., 2016. The WACMOS-ET project - Part 2: Evaluation of global terrestrial evaporation data sets. Hydrol. Earth Syst. Sci. 20 (2), 823–842. https://doi.org/10.5194/hess-20-823-2016.
Mohammed, G.H., Colombo, R., Middleton, E.M., Rascher, U., van der Tol, C., Nedbal, L., et al., 2019. Remote sensing of solar-induced chlorophyll fluorescence (SIF) in vegetation: 50 years of progress. Remote Sens. Environ. 231, 39. https://doi.org/10.1016/j.rse.2019.04.030.
Mu, Q.Z., Zhao, M.S., Running, S.W., 2011. Improvements to a MODIS global terrestrial evapotranspiration algorithm. Remote Sens. Environ. 115 (8), 1781–1800. https://doi.org/10.1016/j.rse.2011.02.019.
Myneni, R., Knyazikhin, Y., Park, T., 2015. MCD15A3H MODIS/Terra+Aqua Leaf Area Index/FPAR 4-day L4 Global 500m SIN Grid V006. NASA EOSDIS Land Processes DAAC.
Nelson, J., Carvalhais, N., Cuntz, M., Delpierre, N., Knauer, J., Ogée, J., Migliavacca, M., Reichstein, M., Jung, M., 2018. Coupling Water and Carbon Fluxes to Constrain Estimates of Transpiration: The TEA Algorithm. J. Geophys. Res.-Biogeosci. 123 (12), 3617–3632. https://doi.org/10.1029/2018jg004727.
Nelson, J.A., Pérez-Priego, O., Zhou, S., Poyatos, R., Zhang, Y., Blanken, P.D., Gimeno, T. E., Wohlfahrt, G., Desai, A.R., Gioli, B., Limousin, J.-M., Bonal, D., Paul-Limoges, E., Scott, R.L., Varlagin, A., Fuchs, K., Montagnani, L., Wolf, S., Delpierre, N., Berveiller, D., Gharun, M., Belelli Marchesini, L., Gianelle, D., Šigut, L., Mammarella, I., Siebicke, L., Andrew Black, T., Knohl, A., Hörtnagl, L., Magliulo, V., Besnard, S., Weber, U., Carvalhais, N., Migliavacca, M., Reichstein, M., Jung, M., 2020. Ecosystem transpiration and evaporation: Insights from three water flux partitioning methods across FLUXNET sites. Global Change Biol. 26 (12), 6916–6930. https://doi.org/10.1111/gcb.15314.
Niu, Z., He, H., Zhu, G., Ren, X., Zhang, L.i., Zhang, K., Yu, G., Ge, R., Li, P., Zeng, N.a., Zhu, X., 2019. An increasing trend in the ratio of transpiration to total terrestrial evapotranspiration in China from 1982 to 2015 caused by greening and warming. Agr. For. Meteorol. 279, 107701. https://doi.org/10.1016/j.agrformet.2019.107701.
Pagan, B.R., Maes, W.H., Gentine, P., Martens, B., Miralles, D.G., 2019. Exploring the Potential of Satellite Solar-Induced Fluorescence to Constrain Global Transpiration Estimates. Remote Sens. 11 (4), 15. https://doi.org/10.3390/rs11040413.
Paschalis, A., Fatichi, S., Pappas, C., Or, D., 2018. Covariation of vegetation and climate constrains present and future T/ET variability. Environ. Res. Lett. 13 (10), 11. https://doi.org/10.1088/1748-9326/aae267.
Paul-Limoges, E., Damm, A., Hueni, A., Liebisch, F., Eugster, W., Schaepman, M.E., Buchmann, N., 2018. Effect of environmental conditions on sun-induced fluorescence in a mixed forest and a cropland. Remote Sens. Environ. 219, 310–323. https://doi.org/10.1016/j.rse.2018.10.018.
Ran, L.M., Pleim, J., Song, C.H., Band, L., Walker, J.T., Binkowski, F.S., 2017. A photosynthesis-based two-leaf canopy stomatal conductance model for meteorology and air quality modeling with WRF/CMAQ PX LSM. J. Geophys. Res.-Atmos. 122 (3), 1930–1952. https://doi.org/10.1002/2016jd025583.
Savitzky, A., Golay, M.J.E., 1964. Smoothing and Differentiation of Data by Simplified Least Squares Procedures. Anal. Chem. 36 (8), 1627–1639. https://doi.org/10.1021/ac60214a047.
Scanlon, T.M., Kustas, W.P., 2010. Partitioning carbon dioxide and water vapor fluxes using correlation analysis. Agr. For. Meteorol. 150 (1), 89–99. https://doi.org/10.1016/j.agrformet.2009.09.005.
Schlesinger, W.H., Jasechko, S., 2014. Transpiration in the global water cycle. Agr. For. Meteorol. 189, 115–117. https://doi.org/10.1016/j.agrformet.2014.01.011.
Scott, R.L., Biederman, J.A., 2017. Partitioning evapotranspiration using long-term carbon dioxide and water vapor fluxes. Geophys. Res. Lett. 44 (13), 6833–6840. https://doi.org/10.1002/2017gl074324.
Sellers, P.J., Berry, J.A., Collatz, G.J., Field, C.B., Hall, F.G., 1992. Canopy reflectance, photosynthesis, and transpiration. III. A reanalysis using improved leaf models and a new canopy integration scheme. Remote Sens. Environ. 42 (3), 187–216. https://doi.org/10.1016/0034-4257(92)90102-P.
Senay, G.B., Bohms, S., Singh, R.K., Gowda, P.H., Velpuri, N.M., Alemu, H., Verdin, J.P., 2013. Operational evapotranspiration mapping using remote sensing and weather datasets: A new parameterization for the SSEB approach. J. Am. Water Resour. As. 49 (3), 577–591. https://doi.org/10.1111/jawr.12057.
Shan, N., Ju, W., Migliavacca, M., Martini, D., Guanter, L., Chen, J., Goulas, Y., Zhang, Y., 2019. Modeling canopy conductance and transpiration from solar-induced chlorophyll fluorescence. Agr. For. Meteorol. 268, 189–201. https://doi.org/10.1016/j.agrformet.2019.01.031.
Shan, N., Zhang, Y., Chen, J.M., Ju, W., Migliavacca, M., Peñuelas, J., Yang, X.i., Zhang, Z., Nelson, J.A., Goulas, Y., 2021. A model for estimating transpiration from remotely sensed solar-induced chlorophyll fluorescence. Remote Sens. Environ. 252, 112134. https://doi.org/10.1016/j.rse.2020.112134.
Song, L., Guanter, L., Guan, K., You, L., Huete, A., Ju, W., Zhang, Y., 2018. Satellite sun-induced chlorophyll fluorescence detects early response of winter wheat to heat stress in the Indian Indo-Gangetic Plains. Global Change Biol 24 (9), 4023–4037. https://doi.org/10.1111/gcb.14302.
Sprintsin, M., Chen, J.M., Desai, A., Gough, C.M., 2012. Evaluation of leaf-to-canopy upscaling methodologies against carbon flux data in North America. J. Geophys. Res.-Biogeosci. 117 https://doi.org/10.1029/2010jg001407.
Stoy, P.C., El-Madany, T.S., Fisher, J.B., Gentine, P., Gerken, T., Good, S.P., Klosterhalfen, A., Liu, S., Miralles, D.G., Perez-Priego, O., Rigden, A.J., Skaggs, T.H., Wohlfahrt, G., Anderson, R.G., Coenders-Gerrits, A.M.J., Jung, M., Maes, W.H., Mammarella, I., Mauder, M., Migliavacca, M., Nelson, J.A., Poyatos, R., Reichstein, M., Scott, R.L., Wolf, S., 2019. Reviews and syntheses: Turning the challenges of partitioning ecosystem evaporation and transpiration into opportunities. Biogeosciences. 16 (19), 3747–3775. https://doi.org/10.5194/bg-16-3747-2019.
Su, Z., 2002. The Surface Energy Balance System (SEBS) for estimation of turbulent heat fluxes. Hydrol. Earth Syst. Sc. 6 (1), 85–100. https://doi.org/10.5194/hess-6-85-2002.
Sun, X.M., Wilcox, B.P., Zou, C.B., 2019. Evapotranspiration partitioning in dryland ecosystems: A global meta-analysis of in situ studies. J. Hydrol. 576, 123–136. https://doi.org/10.1016/j.jhydrol.2019.06.022.
Sun, Y., Frankenberg, C., Wood, J.D., Schimel, D.S., Jung, M., Guanter, L., Drewry, D.T., Verma, M., Porcar-Castell, A., Griffis, T.J., Gu, L., Magney, T.S., Köhler, P., Evans, B., Yuen, K., 2017. OCO-2 advances photosynthesis observation from space via solar-induced chlorophyll fluorescence. Science. 358 (6360) https://doi.org/10.1126/science.aam5747.
Talsma, C.J., Good, S.P., Jimenez, C., Martens, B., Fisher, J.B., Miralles, D.G., McCabe, M. F., Purdy, A.J., 2018. Partitioning of evapotranspiration in remote sensing-based

models. Agr. For. Meteorol. 260, 131–143. https://doi.org/10.1016/j.agrformet.2018.05.010.
Trenberth, K.E., Fasullo, J.T., Kiehl, J., 2009. EARTH'S GLOBAL ENERGY BUDGET. Bull. Am. Meteorol. Soc. 90 (3), 311–323. https://doi.org/10.1175/2008bams2634.1.
van Dijk, A.I.J.M., Gash, J.H., van Gorsel, E., Blanken, P.D., Cescatti, A., Emmel, C., Gielen, B., Harman, I.N., Kiely, G., Merbold, L., Montagnani, L., Moors, E., Sottocornola, M., Varlagin, A., Williams, C.A., Wohlfahrt, G., 2015. Rainfall interception and the coupled surface water and energy balance. Agr. For. Meteorol. 214-215, 402–415. https://doi.org/10.1016/j.agrformet.2015.09.006.
Wang-Erlandsson, L., Van Der Ent, R.J., Gordon, L.J., Savenije, H.H.G., 2014. Contrasting roles of interception and transpiration in the hydrological cycle–Part 1: Temporal characteristics over land. Earth Syst. Dynam. 5 (2), 441–469. https://doi.org/10.5194/esd-5-441-2014.
Wang, K., Dickinson, R.E., 2012. A review of global terrestrial evapotranspiration: Observation, modeling, climatology, and climatic variability. Rev. Geophys. 50 (2) https://doi.org/10.1029/2011RG000373.
Wang, L.X., Good, S.P., Caylor, K.K., 2014. Global synthesis of vegetation control on evapotranspiration partitioning. Geophys. Res. Lett. 41 (19), 6753–6757. https://doi.org/10.1002/2014gl061439.
Wei, Z.W., Lee, X.H., Wen, X.F., Xiao, W., 2018. Evapotranspiration partitioning for three agro-ecosystems with contrasting moisture conditions: a comparison of an isotope method and a two-source model calculation. Agr. For. Meteorol. 252, 296–310. https://doi.org/10.1016/j.agrformet.2018.01.019.
Wei, Z.W., Yoshimura, K., Okazaki, A., Kim, W., Liu, Z.F., Yokoi, M., 2015. Partitioning of evapotranspiration using high-frequency water vapor isotopic measurement over a rice paddy field. Water Resour. Res. 51 (5), 3716–3729. https://doi.org/10.1002/2014wr016737.
Wei, Z.W., Yoshimura, K., Yang, L.X., Miralles, D.G., Jasechko, S., Lee, X.H., 2017. Revisiting the contribution of transpiration to global terrestrial evapotranspiration. Geophys. Res. Lett. 44 (6), 2792–2801. https://doi.org/10.1002/2016gl072235.
Wutzler, T., Lucas-Moffat, A., Migliavacca, M., Knauer, J., Sickel, K., Šigut, L., Menzer, O., Reichstein, M., 2018. Basic and extensible post-processing of eddy covariance flux data with REddyProc. Biogeosciences. 15 (16), 5015–5030. https://doi.org/10.5194/bg-15-5015-2018.
Xia, Y., Mitchell, K., Ek, M., Sheffield, J., Cosgrove, B., Wood, E., Luo, L., Alonge, C., Wei, H., Meng, J., Livneh, B., Lettenmaier, D., Koren, V., Duan, Q., Mo, K., Fan, Y., Mocko, D., 2012. Continental-scale water and energy flux analysis and validation for the North American Land Data Assimilation System project phase 2 (NLDAS-2): 1. Intercomparison and application of model products: WATER AND ENERGY FLUX ANALYSIS. J. Geophys. Res. 117 (D3) https://doi.org/10.1029/2011JD016048.
Yang, H., Yang, X.i., Zhang, Y., Heskel, M.A., Lu, X., Munger, J.W., Sun, S., Tang, J., 2017. Chlorophyll fluorescence tracks seasonal variations of photosynthesis from leaf to canopy in a temperate forest. Global Change Biol. 23 (7), 2874–2886. https://doi.org/10.1111/gcb.13590.
Yang, M.H., Zuo, R.T., Wang, L.Q., Chen, X., 2018. A simulation study of global evapotranspiration components using the community land model. Atmosphere. 9 (5), 178. https://doi.org/10.3390/atmos9050178.
Yang, X., Tang, J., Mustard, J.F., Lee, J.-E., Rossini, M., Joiner, J., Munger, J.W., Kornfeld, A., Richardson, A.D., 2015. Solar-induced chlorophyll fluorescence that correlates with canopy photosynthesis on diurnal and seasonal scales in a temperate deciduous forest. Geophys. Res. Lett. 42 (8), 2977–2987. https://doi.org/10.1002/2015gl063201.
Yoshida, Y., Joiner, J., Tucker, C., Berry, J., Lee, J.-E., Walker, G., Reichle, R., Koster, R., Lyapustin, A., Wang, Y., 2015. The 2010 Russian drought impact on satellite measurements of solar-induced chlorophyll fluorescence: Insights from modeling and comparisons with parameters derived from satellite reflectances. Remote Sens. Environ. 166, 163–177. https://doi.org/10.1016/j.rse.2015.06.008.
Yoshimura, K., Miyazaki, S., Kanae, S., Oki, T., 2006. Iso-MATSIRO, a land surface model that incorporates stable water isotopes. Global Planet. Change. 51 (1–2), 90–107. https://doi.org/10.1016/j.gloplacha.2005.12.007.
Yue, K., De Frenne, P., Fornara, D.A., Van Meerbeek, K., Li, W., Peng, X., Ni, X., Peng, Y., Wu, F., Yang, Y., Peñuelas, J., 2021. Global patterns and drivers of rainfall partitioning by trees and shrubs. Global Change Biol. 27 (14), 3350–3357. https://doi.org/10.1111/gcb.15644.
Zahn, E., Bou-Zeid, E., Good, S.P., Katul, G.G., Thomas, C.K., Ghannam, K., et al., 2022. Direct partitioning of eddy-covariance water and carbon dioxide fluxes into ground and plant components. Agr. For. Meteorol. 315: 108790. https://doi.org/10.1016/j.agrformet.2021.108790.
Zeng, Z., Piao, S., Li, L.Z.X., Zhou, L., Ciais, P., Wang, T., Li, Y., Lian, X.u., Wood, E.F., Friedlingstein, P., Mao, J., Estes, L.D., Myneni, R., Peng, S., Shi, X., Seneviratne, S.I., Wang, Y., 2017. Climate mitigation from vegetation biophysical feedbacks during the past three decades. Nat. Clim. Change. 7 (6), 432–436. https://doi.org/10.1038/nclimate3299.
Zeng, Z.Z., Wang, T., Zhou, F., Ciais, P., Mao, J.F., Shi, X.Y., Piao, S.L., 2014. A worldwide analysis of spatiotemporal changes in water balance-based evapotranspiration from 1982 to 2009. J. Geophys. Res.-Atmos. 119 (3), 1186–1202. https://doi.org/10.1002/2013JD020941.
Zhang, K., Kimball, J.S., Running, S.W., 2016a. A review of remote sensing based actual evapotranspiration estimation. Wiley Interdiscip. Rev.-Water. 3 (6), 834–853. https://doi.org/10.1002/wat2.1168.
Zhang, K., Zhu, G.F., Ma, J.Z., Yang, Y.T., Shang, S.S., Gu, C.J., 2019a. Parameter Analysis and Estimates for the MODIS Evapotranspiration Algorithm and Multiscale Verification. Water Resour. Res. 55 (3), 2211–2231. https://doi.org/10.1029/2018wr023485.
Zhang, Y.Q., Kong, D.D., Gan, R., Chiew, F.H.S., McVicar, T.R., Zhang, Q., Yang, Y.T., 2019b. Coupled estimation of 500 m and 8-day resolution global evapotranspiration and gross primary production in 2002–2017. Remote Sens. Environ. 222, 165–182. https://doi.org/10.1016/j.rse.2018.12.031.
Zhang, Y., Peña-Arancibia, J.L., McVicar, T.R., Chiew, F.H.S., Vaze, J., Liu, C., Lu, X., Zheng, H., Wang, Y., Liu, Y.Y., Miralles, D.G., Pan, M., 2016b. Multi-decadal trends in global terrestrial evapotranspiration and its components. Sci. Rep. 6 (1) https://doi.org/10.1038/srep19124.
Zhang, Z.Y., Chen, J.M., Guanter, L., He, L.M., Zhang, Y.G., 2019c. From Canopy-Leaving to Total Canopy Far-Red Fluorescence Emission for Remote Sensing of Photosynthesis: First Results From TROPOMI. Geophys. Res. Lett. 46 (21), 12030–12040. https://doi.org/10.1029/2019gl084832.
Zhou, S., Yu, B.F., Zhang, Y., Huang, Y.F., Wang, G.Q., 2016. Partitioning evapotranspiration based on the concept of underlying water use efficiency. Water Resour. Res. 52 (2), 1160–1175. https://doi.org/10.1002/2015WR017766.